WFPS-TME-042
DATE - AUGUST, 1977

WESTINGHOUSE COMPACT POLOIDAL DIVERTOR REFERENCE DESIGN FOR TNS

fusion power
systems department

Westinghouse Electric Corporation
P.O. Box 10864, Pgh. Pa. 15236

DISCLAIMER

WFPS-TME-042
DATE - AUGUST, 1977

WESTINGHOUSE COMPACT POLOIDAL DIVERTOR REFERENCE DESIGN

Prepared by: Tien-Fang Yang, A. Y. Lee, G. W. Ruck

Tien-Fang Yang
A. Y. Lee
G. W. Ruck

Approved by: G. Gibson

G. Gibson, Manager
Plasma Engineering

Approved by: T. C. Varljen

T. C. Varljen, Manager
TNS Engineering

Approved by: C. A. Flanagan

C. A. Flanagan, Manager
TNS Project

Westinghouse Electric Corporation

Fusion Power Systems Department,
P.O. Box 10864, Pgh. Pa. 15236

ACKNOWLEDGEMENT

This work was performed for the Oak Ridge National Laboratory Fusion Energy Division, under U.S. Energy Research and Development Administration Contract W-7405-ENG-26, Subcontract 7117. Reproduction, translation, publication, use and disposal, in whole or in part, by or for the United States Government is permitted.

LEGAL NOTICE

FOREWORD

The Division of Magnetic Fusion Energy within the U.S. Energy Research and Development Administration has initiated within the fusion development program for tokamak power reactors a series of systems studies aimed at the definition of subsequent generations of tokamak devices leading to a commercial prototype reactor. Since April, 1976, a design team composed of representatives from the ORNL Fusion Energy Division and the Westinghouse Fusion Power Systems Department has been engaged in scoping studies associated with the definition of The Next Step (TNS) in the tokamak program after the TFTR. Provisional goals established for TNS include:

- achievement of ignition
- demonstration of burning dynamics
- evaluation of design requirements and solutions for long pulse operation
- features which extrapolate to a viable power reactor
- availability in the mid-to-late 1980's

It is in this context that the work reported herein was performed.

ABSTRACT

A feasible compact poloidal divertor system has been designed as an impurity control and vacuum vessel first-wall protection option for the TNS tokamak. A divertor is not presently used in any of the reference design approaches under study by the ORNL/Westinghouse team; however, this evaluation has developed a feasible concept which may be implemented without major impact on the overall size of the tokamak. The divertor coils are inside the TF coil array and vacuum vessel. The poloidal divertor is formed by a pair of coil sets with zero net current. Each set consists of a number of coils forming a dish-shaped washer-like ring. The magnetic flux in the space between the coil sets is compressed vertically to limit the height and to expand the horizontal width of the particle and energy burial chamber which is located in the gap between the coil sets. The intensity of the poloidal field is increased to make the pitch angle of the flux lines very large so that the diverted particles can be intercepted by a large number of panels oriented at a small angle with respect to the flux lines. They are carefully shaped and designed such that the entire surfaces are exposed to the incident particles and are not shadowed by each other. Large collecting surface areas can be obtained. Flowing liquid lithium film and solid metal panels have been considered as the particle collectors. The power density for the former is designed at 1 MW/m^2 and for the latter 0.5 MW/m^2. The major mechanical, thermal, and vacuum problems have been evaluated in sufficient detail so that the advantages and difficulties are identified. A complete functional picture is presented. The lithium film has the advantage of being renewable but is complicated by mechanical piping and an electrical network to provide lithium pumping. The solid getters operate at lower power density, but can trap helium. This divertor model is independent of a particular tokamak system; although the analyses performed were based on TNS.

TABLE OF CONTENTS

LIST OF FIGURES

LIST OF FIGURES (CONTINUED)

LIST OF TABLES

1.0 INTRODUCTION

The poloidal divertor is considered as one option for impurity control and first-wall protection by removing the charged particles diffused from the plasma in the TNS trade study[1]. This work is devoted to the examination of those factors which contribute to a sound physical basis for obtaining a feasible engineering design of a magnetic divertor. A sufficiently detailed and complete design effort has been carried out to understand the most important aspects of this design. A conceptual design, the difficulties, the possible uncertainties, as well as the advantages of this system are presented.

This report concentrates on the "so-called" natural poloidal divertor configuration[2], where the divertor and equilibrium field (EF) coils are inside the toroidal field (TF) coils. It is generally conceded that to operate a tokamak at steady state or for long burning times, a divertor with a high efficiency particle trapping system may be necessary to reduce 1) the impurities from the first-wall, and 2) the gas throughput to the pumping system to a reasonable level. This argument, however, does not preclude the possibility of finding a method of recycling the particles and protecting the first-wall to reduce the impurities so that the plasma can sustain a reasonably long period of steady operation. Our concern here, assuming a magnetic divertor is proven to be necessary, is to find a design approach which is feasible from both theoretical and engineering considerations. Considerable attention has been focused on poloidal divertors[3-23] and their advantages and difficulties have been identified. The advantages are: 1) that the poloidal divertor is a natural result of having a poloidal field to maintain plasma equilibrium; and 2) that it will maintain the axisymmetric configuration of the tokamak. The disadvantages are: 1) that the power deposition on the particle collecting surfaces tend to be very high; 2) that the engineering problems associated with the divertor coils and particle collection tend to be very difficult; 3) pumping requirements are still very high; and 4) that there is yet no conclusive experimental evidence to support the assumed capability of the poloidal divertor.

It has been theoretically proven by Mense, Keilhaker, and others that the unloading efficiency of the poloidal divertor is better than 98%[15,16] and the shielding efficiency is better than 96%[15]. Hopefully, confirmatory experimental results will be obtained from the PDX experiment[8]. The prospect of the poloidal divertor would be enhanced if reasonable particle collecting methods can be found. For this purpose, we discuss a concept and a method of designing the magnetic flux pattern and component configuration which will provide sufficient collecting area to keep the average power deposition below 1 MW/m^2, while the height of the system is minimized. The idea is to compress the magnetic flux vertically in the particle burial region instead of expanding in the usual way, so that the vertical dimension is limited and horizontal width is increased. The method of collection will be discussed in detail in the following sections.

Two particle gettering methods were considered in our study. One is the well discussed liquid lithium free gravity fall[4] and liquid lithium flow over gold plated, stainless steel screens[18,23]. When chevron structures are used[23], 99.9% gettering efficiency for hydrogen isotopes has been claimed. However, the physical and thermal properties of liquid lithium flow in a strong magnetic field are not known and the piping and electric network required to pump the lithium is found to be very complicated in this study. This led to a serious evaluation of solid getters. The thermal load for this divertor can be designed as low as 0.5 MW/m^2 in the TNS application; therefore, solid getters now become possible or even competitive because helium ions can also be trapped.

The following sections discuss 1) this divertor concept, and 2) the major components of mechanical design, the thermal design, the lithium getter system, the solid getter system, and vacuum design considerations. The advantages and disadvantages are indicated and recommendations for further study are provided.

2.0 PHYSICAL CONCEPT

In this section we discuss the design of the divertor magnetic field pattern so as to provide sufficient area for particle collection and sufficient space for shielding. Candidate particle collection methods are identified and described. The MHD equilibrium calculation of the flux pattern and the other analyses are based on a typical TNS-3 tokamak model[1,2,26]. This designation applies to one of a series of point designs under consideration in the ORNL/Westinghouse TNS study. TNS-3 refers to a set of tokamaks using NbTi superconducting TF coils. The key plasma parameters associated with the typical design point chosen for the divertor study are given in Table 2-1.

2.1 DIVERTOR MAGNETIC FIELD DESIGN

The preliminary magnetic field design by Peng[26] for TNS provides for three sets of poloidal field windings to control and shape the plasma to attain high beta equilibria. From stability considerations a D-shaped plasma cross section was found to be desirable and, in the process of determining the required distribution of windings, it was found that a particular arrangement of turns led to a natural poloidal field divertor configuration with fluxes near the null point of the D cross section as shown in Figure 2-1. The EF coil system typically consists of inner EF coils, outer EF coils, and divertor-like coils. The parameters of the reference coil set are given in Table 2-2 for TNS-3 for the natural divertor configuration. Incidentally, alternate designs for the TNS-3 without the natural divertor are quite similar so that it appears that this feature has little engineering impact.

Starting with the configuration of Figure 2-1, the present study considered the possibility of implementing a divertor system within the geometry shown, and with a single divertor coil. This was not found to be practical for the following reasons: 1) there is not enough space to provide nuclear shielding for the coil and to supply coolant to the coil; 2) the burial chamber for the divertor will be

TABLE 2-1

KEY PLASMA PARAMETERS FOR A TYPICAL TNS POINT DESIGN

Plasma Major Radius	R_o = 5 m
Plasma Minor Radius	a = 1.25 m
Toroidal Field on Axis	B_o = 4 T
Elongation	ε = 1.6
Plasma Current	I_p = 6.4 MA
Average Beta*	$\bar{\beta}$ = 14.7 %
Equivalent throughput to Divertor	Q_p = 1500 torr liter/sec $\cong$ 5 x 10^{22} particles/sec
Thermal Power to Divertor	Q_T = 320 MW
Total Fusion Power Generated (21 MeV/Reaction)	1900 MW
Plasma Ion Temperature	$\bar{T}_i$ = 13.5 keV
Energy Containment Time	τ_E = 1.2 s
Plasma Ion Density	$\bar{n}_i$ = 2 x 10^{20} m^{-3}

* Highest average β considered in the TNS trade studies. In general, devices were analyzed in which β varied from 5 to 15%.

TABLE 2-2

CURRENTS AND LOCATIONS OF THE EF COILS WITH A NATURAL DIVERTOR FOR A TYPICAL TNS-3 POINT DESIGN

No.	R(m)	Z(m)	Typical Amp-Turns/I_p*	
1	3.15	0.21	-0.042	(EF-I)
2	3.17	0.65	-0.042	
3	3.25	1.26	-0.042	
4	3.51	2.02	-0.042	
5	4.00	2.59	+0.13	(EF-D)
6	4.90	2.55	-0.093	(EF-O)
7	5.75	2.10	-0.093	
8	6.29	1.51	-0.093	
9	6.63	0.95	-0.093	
10	6.82	0.33	-0.093	

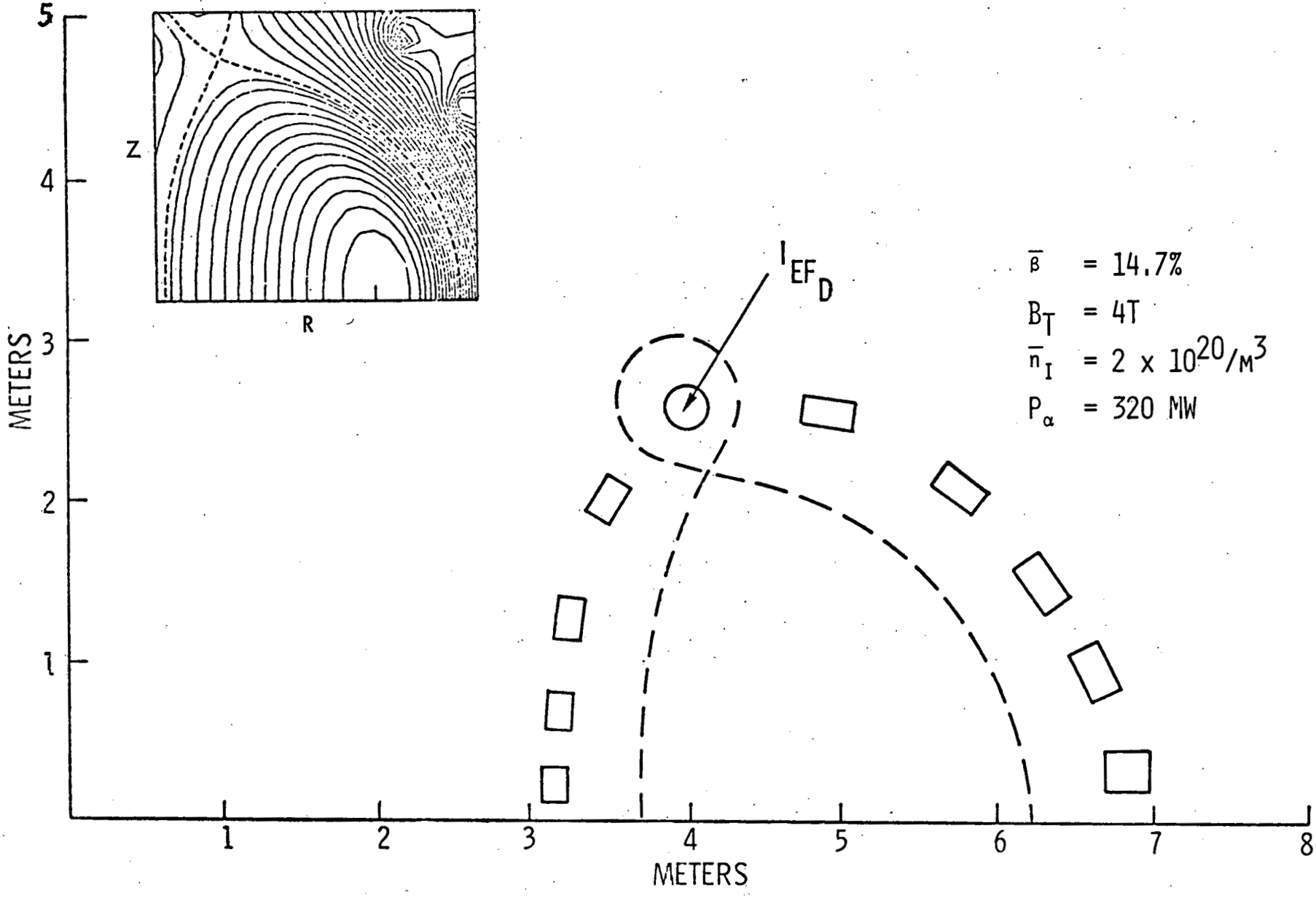

Figure 2-1. Plasma shape of TNS-3 without divertor burial chamber design. The magnetic flux plot of the equilibrium configuration is shown in the upper left corner.

directly exposed to neutrons and the backstreaming of neutrals into the plasma will be large; and 3) the power density on the particle collector is too high because the magnetic flux from the scrape-off layer is not spread sufficiently in the burial chamber. The third reason is the most important and led to consideration of alternate magnetic field geometries.

The essence of the compact poloidal divertor concept is shown in Figure 2-2 where we propose to augment the previous single divertor coil with an array of opposing coil sets which define a magnetic flux slot. The net current of these coil sets is designed to be zero so that they have negligible effect on the plasma. The lower set of coils has positive currents, in the same direction as the current I_{EF-D}, which form a plane passing through the original divertor coil. The upper set of coils has an equivalent negative current. The angle of the current plane with the horizontal is arbitrary and is about 20°, as shown in the figure, to provide maximum utilization of the space. The objective of this design is to form a slot between the two coil sets by compressing the flux instead of expanding it vertically (the usual way to gain area). The height is now reduced, but the width is increased to use as much of the available space as possible.

The burial chamber will be located inside this slot. The slot looks like a dished washer with thickness d and width w. In this model we have d = 0.3 m, w = 1.5 m; the total current in each coil set is I_D = 3.0 MA. The poloidal field intensity B_p in the burial chamber will be about 1.55 T. Thus, the field lines in the slot will have a large pitch angle defined as

$$\alpha = \tan^{-1} \frac{B_p}{B_T} \approx 19° \quad , \qquad (2\text{-}1)$$

The toroidal field strength B_T = 4.6 T at R_D = 4.35 m, the radius of the centerline of the burial chamber. This allows placement of the collecting plate in conformance with the field lines. This provides a large collecting area and also allows adequate space for the structural members and associated hardware.

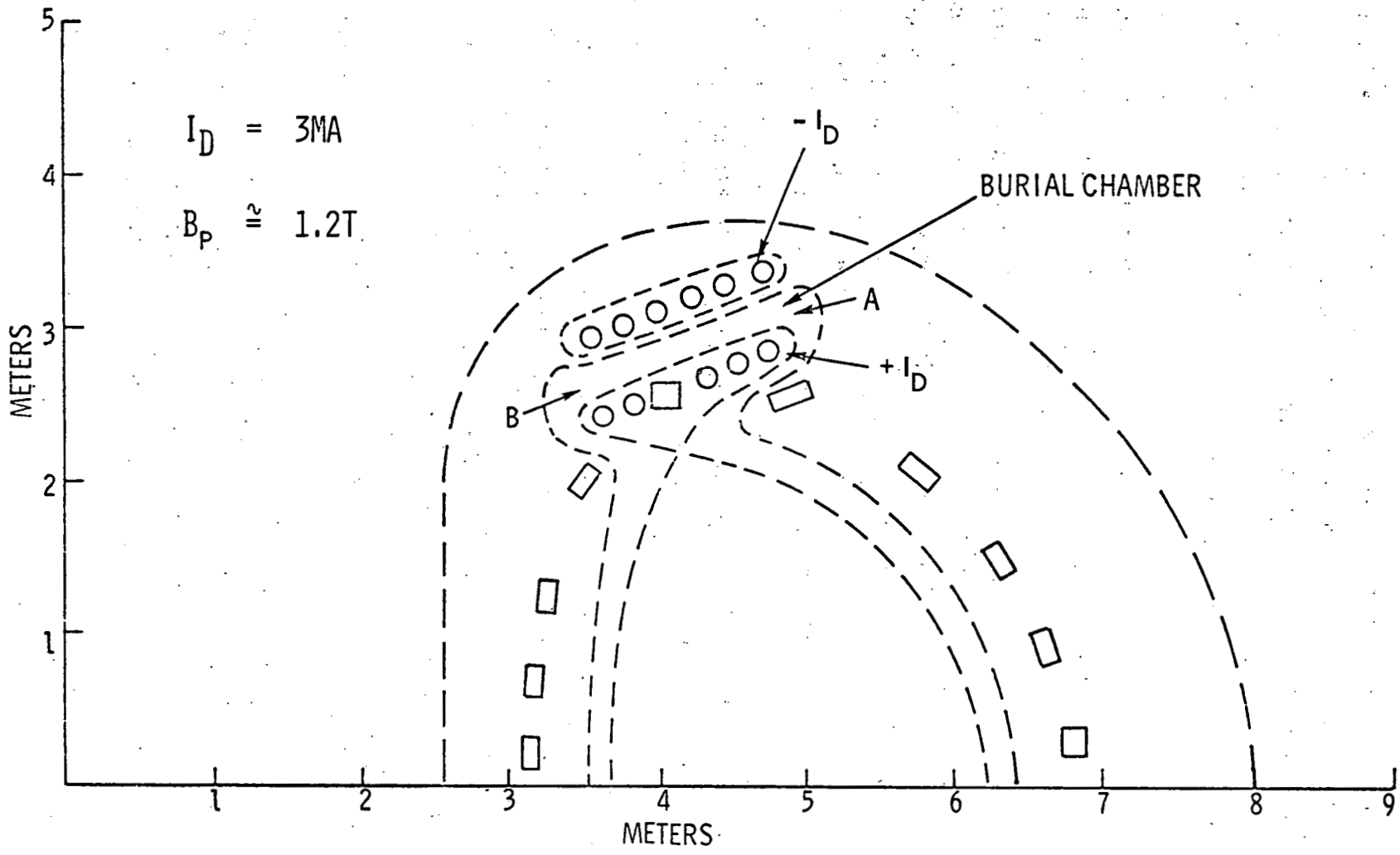

Figure 2-2. Proposed divertor design; flux in the chamber is compressed by two sets of coils.

The MHD equilibrium configuration including the divertor coil sets has been obtained as shown in Figure 2-3. This was calculated for $\bar{\beta} \tilde{=} 1\%$ and for I_p = 3.6 MA. We can expect that the pattern remains the same for high $\bar{\beta}$ because the current I_D remains fixed. The divertor field, as well as the toroidal field, are steady state. There is no additional power handling requirement. The magnetic flux pattern changes very little by making small variations in the current I_D; therefore, we can choose I_D to give B_p = 1.55 T. The perpendicular component of the magnetic stress on the conductor can be calculated from

$$T_{\perp} = \frac{1}{2\mu_o} B_{\perp}^2 \tilde{\approx} 1.0 \times 10^6 \text{ newton/m}^2 \quad . \qquad (2\text{-}2)$$

2.2 PARTICLE COLLECTION METHODS

Let us first illustrate the method of particle collection with lithium. The flux lines in the burial chamber are sketched in Figure 2-4 as viewed from the top. If we arbitrarily divide this flux slab into 48 bundles, the method of collecting the particles is simply to intercept the oncoming particle stream with lithium-wetted screens which are placed at a small angle with respect to the field lines as shown by Figure 2-5, which is the enlargement of a flux bundle AB of Figure 2-4. The concept of collection is illustrated for clarity in this figure. The space behind the screen is available for structure, pumping ports, and a lithium circulating path. All of the structures and coils are protected from the particles by the lithium-wetted screens formed in the shape of a "horn". The lithium screens are placed on the top and bottom of the collecting horns to increase the collecting area. An illustration of two adjacent horns is shown in Figure 2-6. An $\vec{E} \times \vec{B}$ pump for circulating the lithium is represented by the capacitor plates. There are a total of 192 horns in each divertor, which give a total collecting area of $\tilde{\approx}$ 320 m^2. To increase the capture efficiency of the scattered and secondary particles, screens can be inserted into the horn which coincide with the field lines so as not to shadow the collecting surfaces. Increasing the collecting surface can be done by increasing the number of collecting horns.

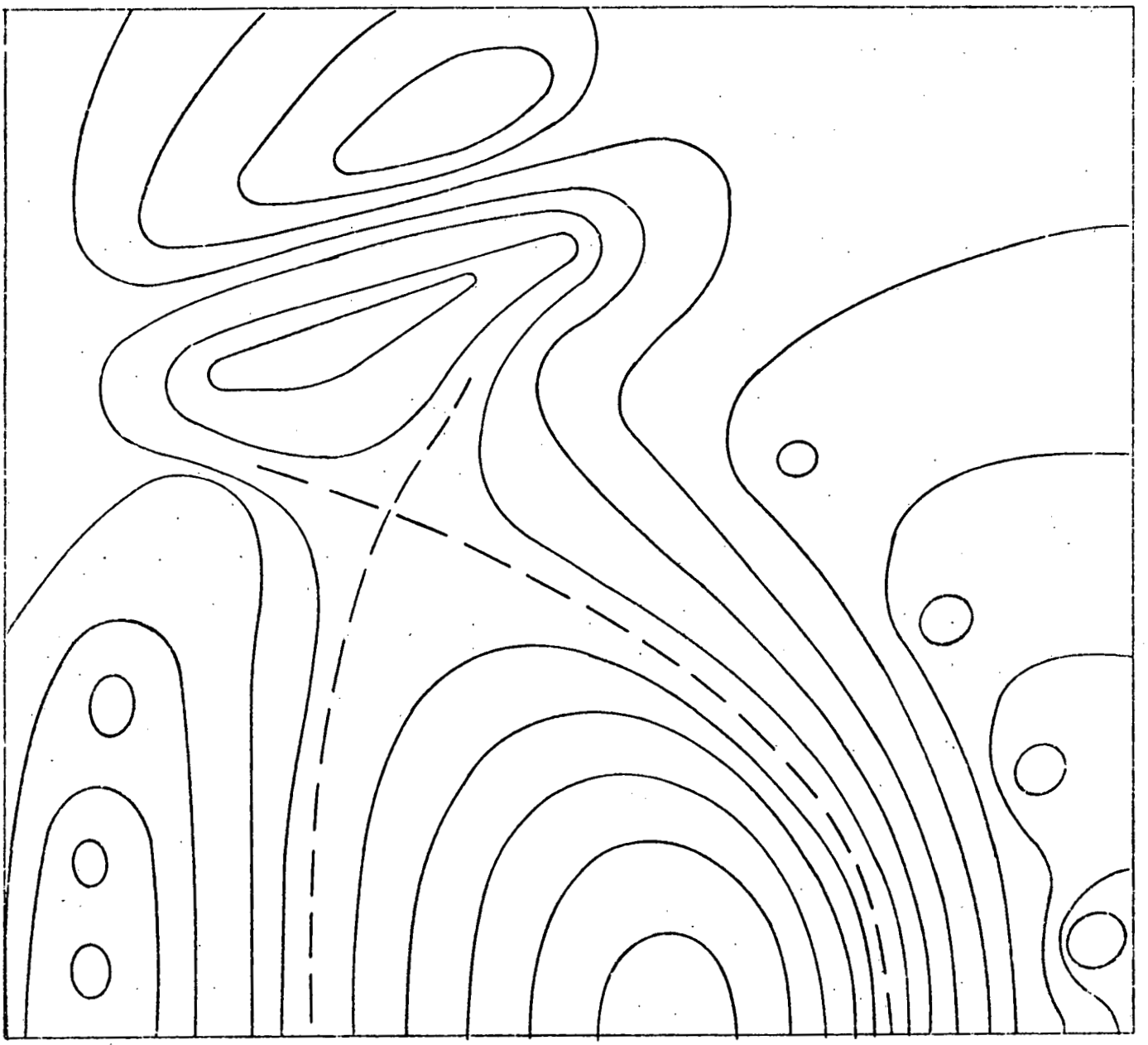

Figure 2-3. The magnetic flux plot of the equilibrium configuration, including the divertor coils. (This is traced from the printer plot and is not accurate.)

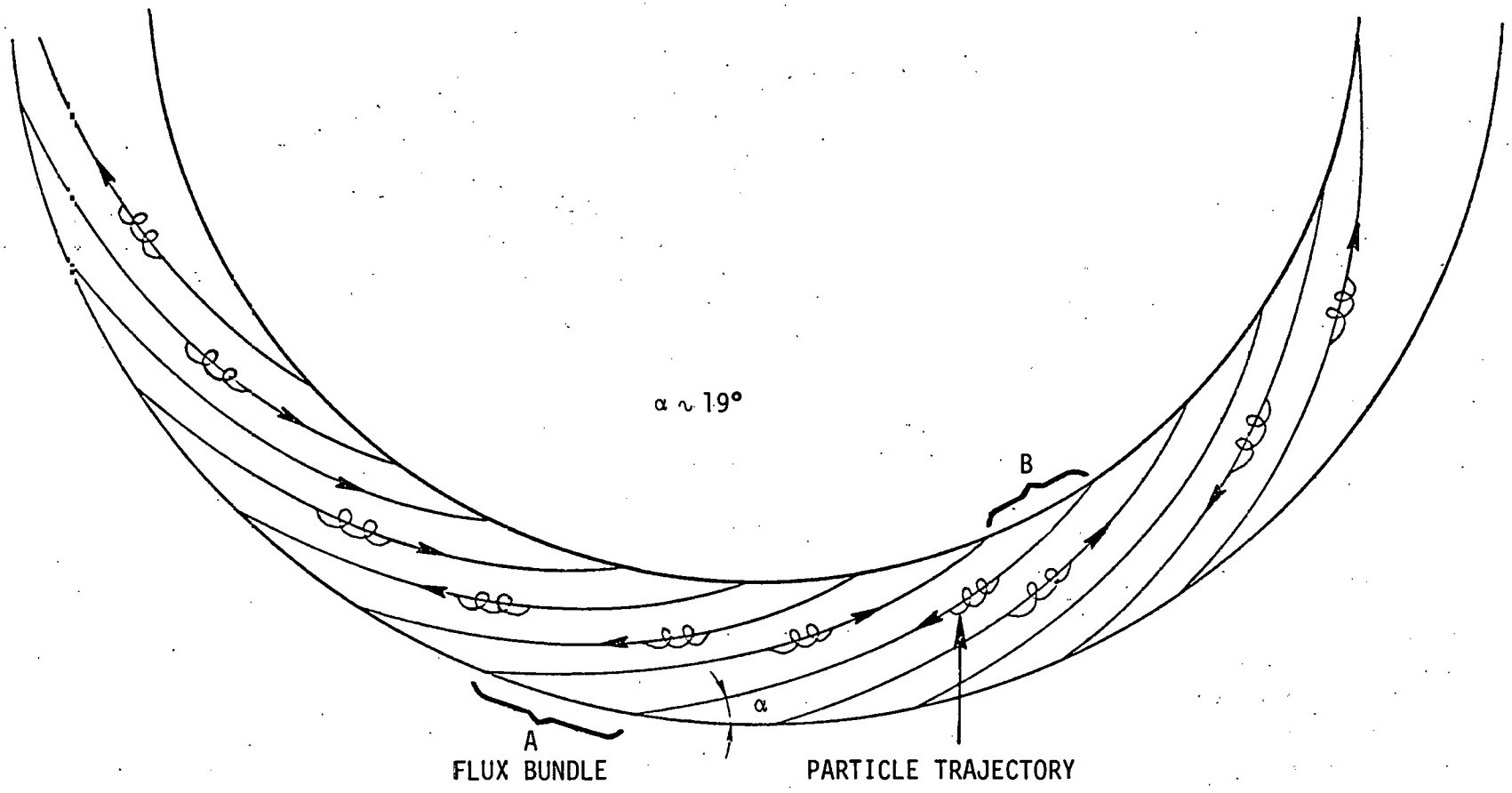

Figure 2-4. Flux and particle motions in the burial chamber (top view of the burial chamber).

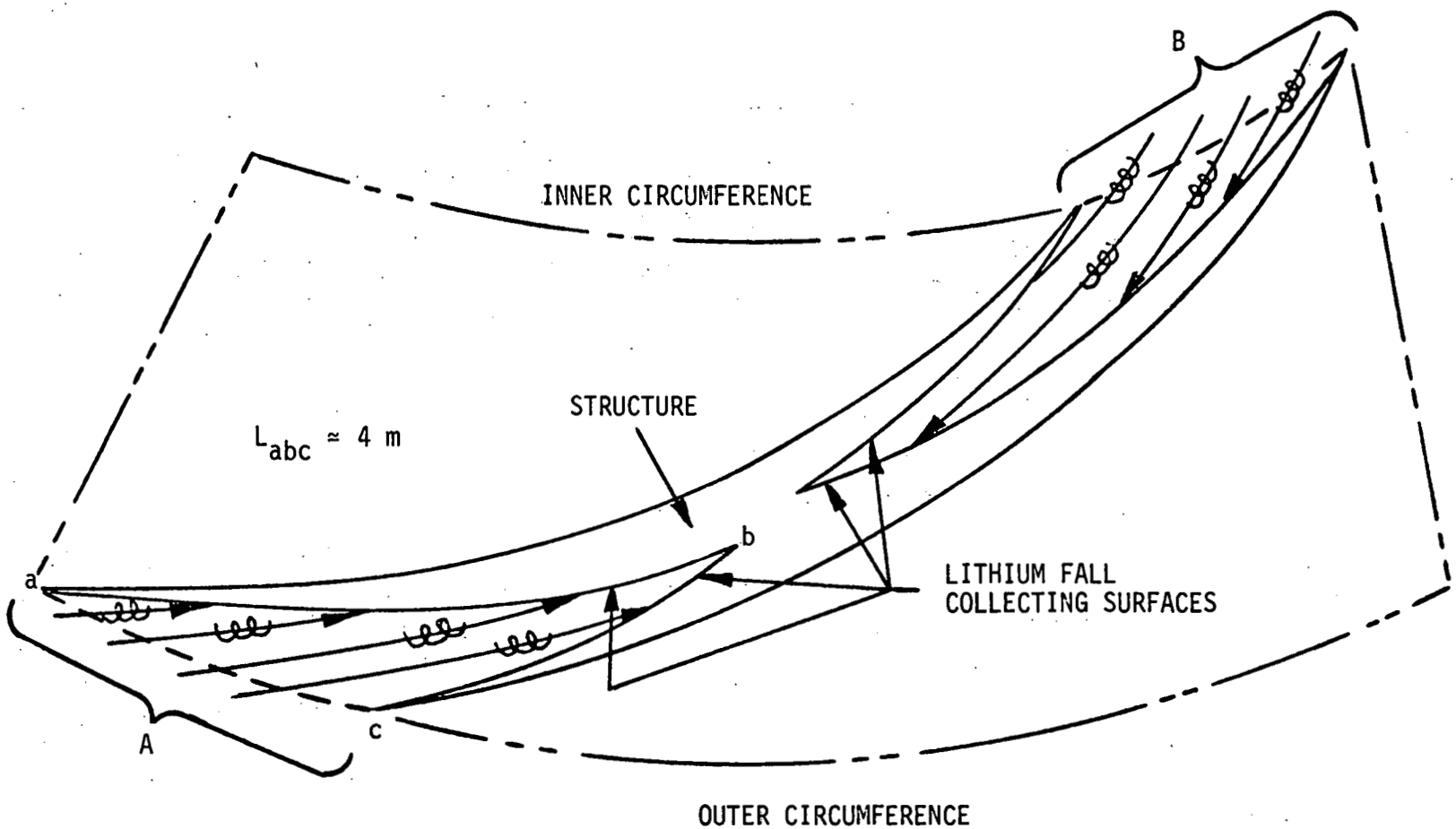

Figure 2-5. Enlargement of the flux bundle, AB, in Figure 2-2. Particles are intercepted by the lithium-wetted surfaces.

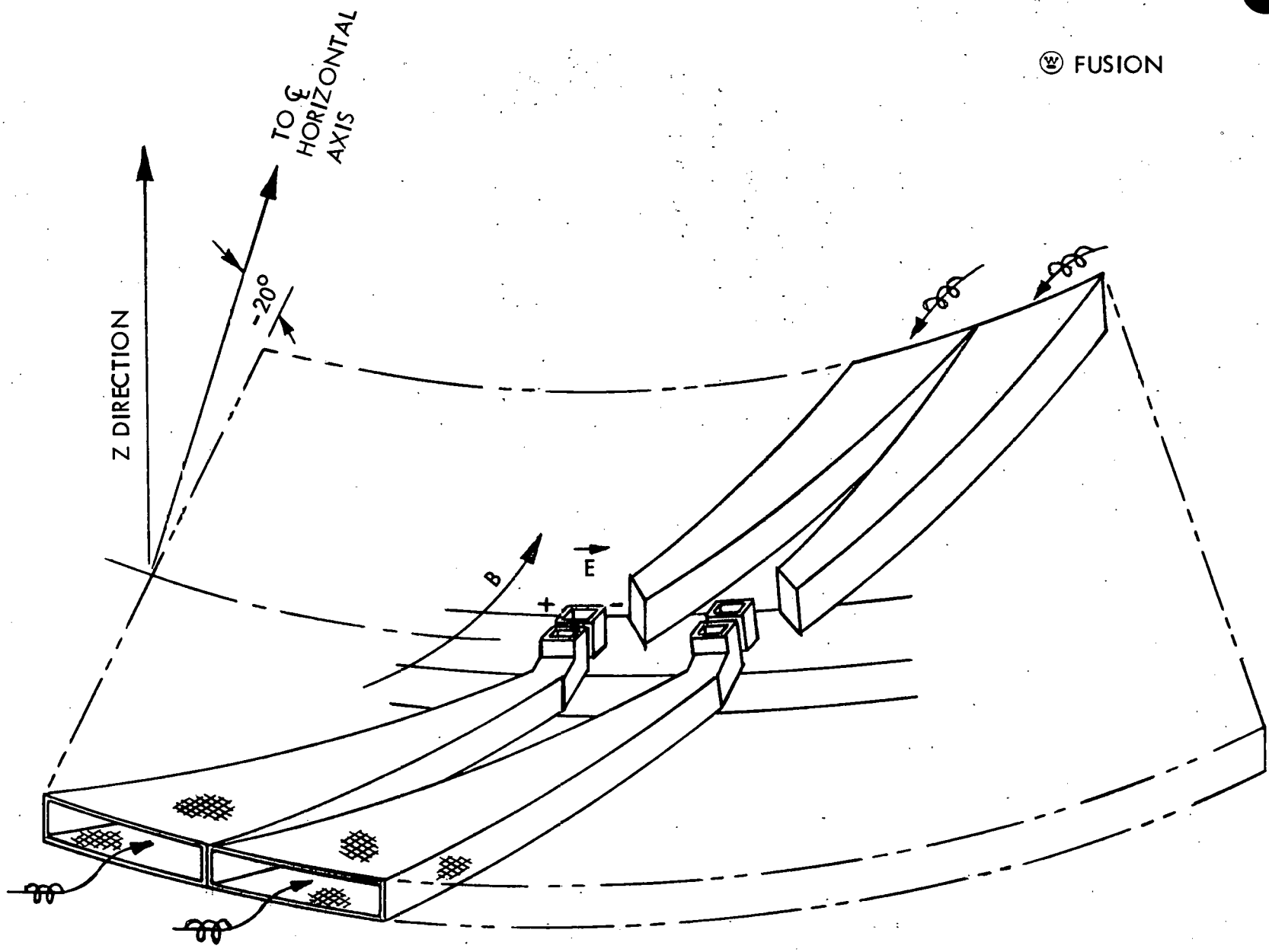

Figure 2-6. Particle collecting horns with liquid lithium collecting screens are shown by the meshes. The lithium is circulated by the $\vec{E} \times \vec{B}$ pumps within the ports.

The characteristics and the design parameters of solid getters are discussed in greater detail in Section 5 on vacuum considerations. For solid getters a much larger surface area is needed to reduce the thermal load and particle flux. For this purpose, we again divide each of the 48 flux bundles into five or more channels as shown in Figure 2-7. The field lines are indicated by dotted curves with arrows. The collecting panels are indicated by solid lines with fins. The surfaces are curved away from the field lines at a small angle in order to intercept the particles. The fins are shadowed by the panels from the incident charged particles and serve only as traps for scattered or secondary neutral particles. This is again illustrated by the enlarged segment ABCD shown in the upper left corner. There are no back-side walls for the horns so that the neutrals that escape the fin trapping will enter and be gettered by the Zr/Al panels behind the horns. An illustration of two adjacent horns is again shown by Figure 2-8. A total surface area of 640 m^2 of titanium is estimated for this arrangement. Therefore, the power density is reduced to 0.5 MW/m^2, which represents a modest heat load. The charged particle getter panel is chosen to be titanium on grounds which are discussed later.

The orientation of the collector horns in the divertor assembly is shown by Figure 2-9. The horn will house solid metal panels or will be lined with lithium-wetted screens as described in the above. The description of the mechanical structure can be found in Section 4.

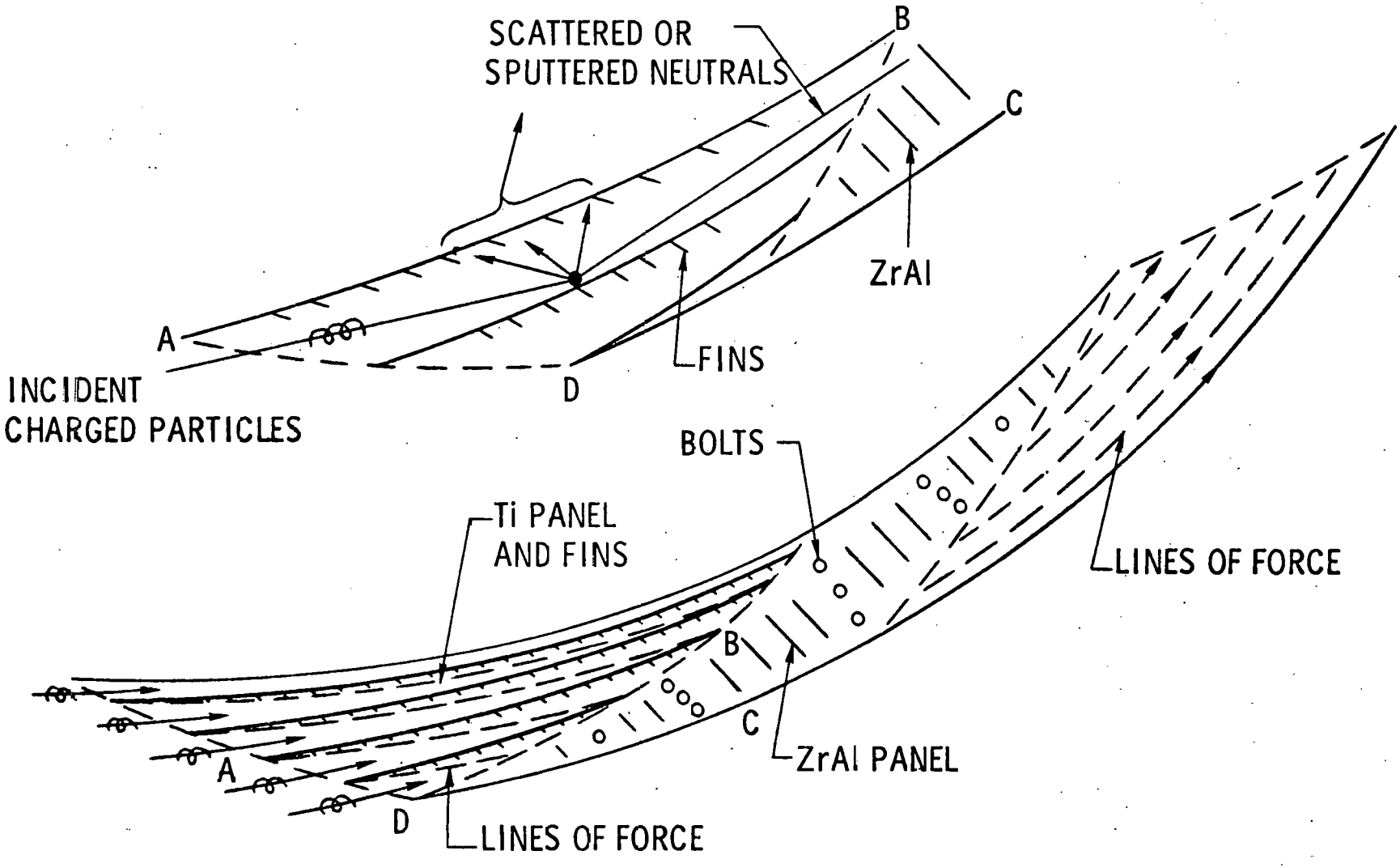

Figure 2-7. Ti and Zr/Al solid getter panels. Ti panels are used to getter ions. The fins on the back are used for trapping scattered and sputtered neutrals. The escaped neutrals are again gettered by Zr/Al panels.

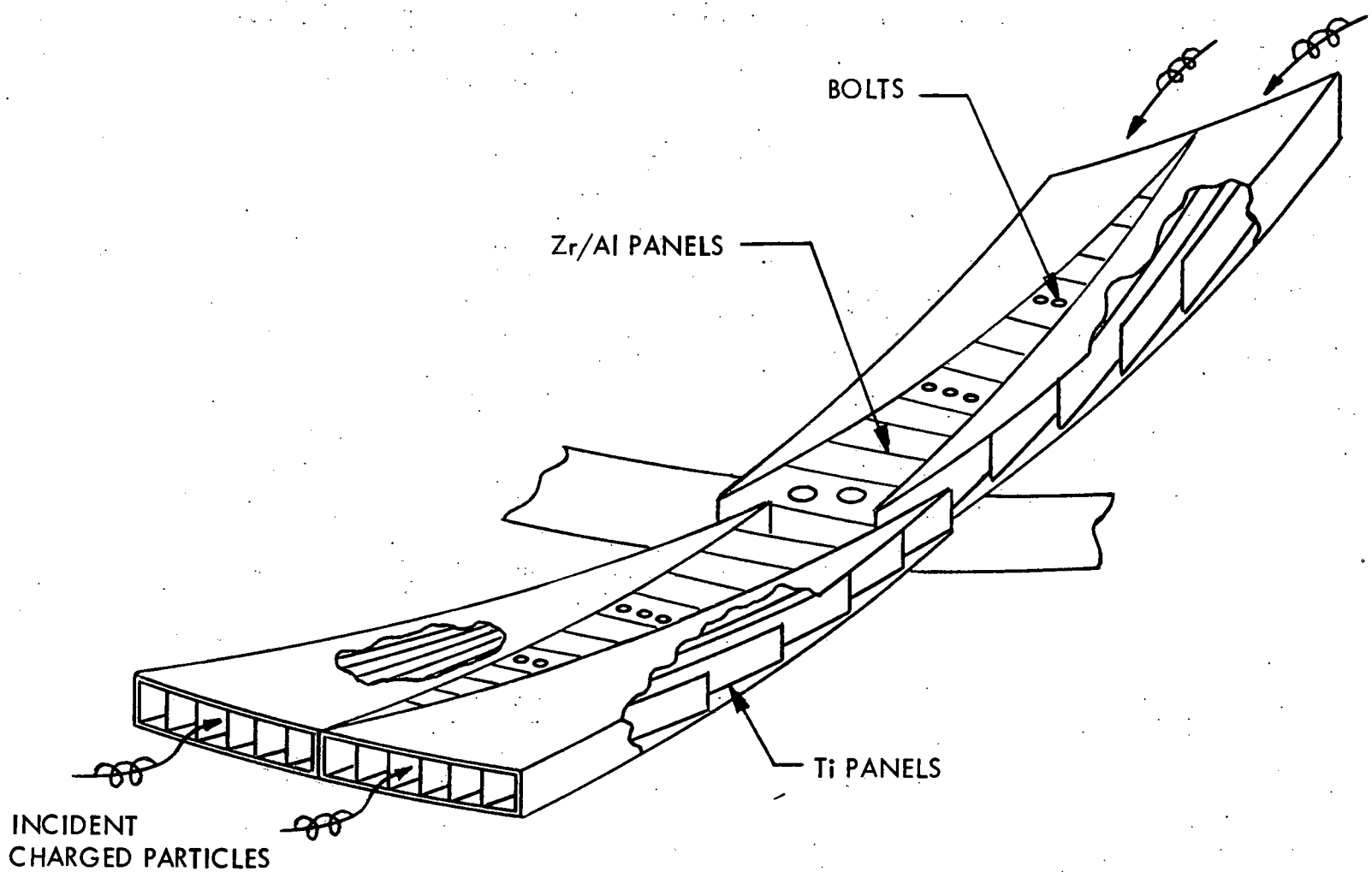

Figure 2-8. Particle collector horns with Ti getter panels. Ti will trap ions (H_2^+, D^+, He^+). The escaped hydrogenic neutrals will be gettered by Zr/Al panels.

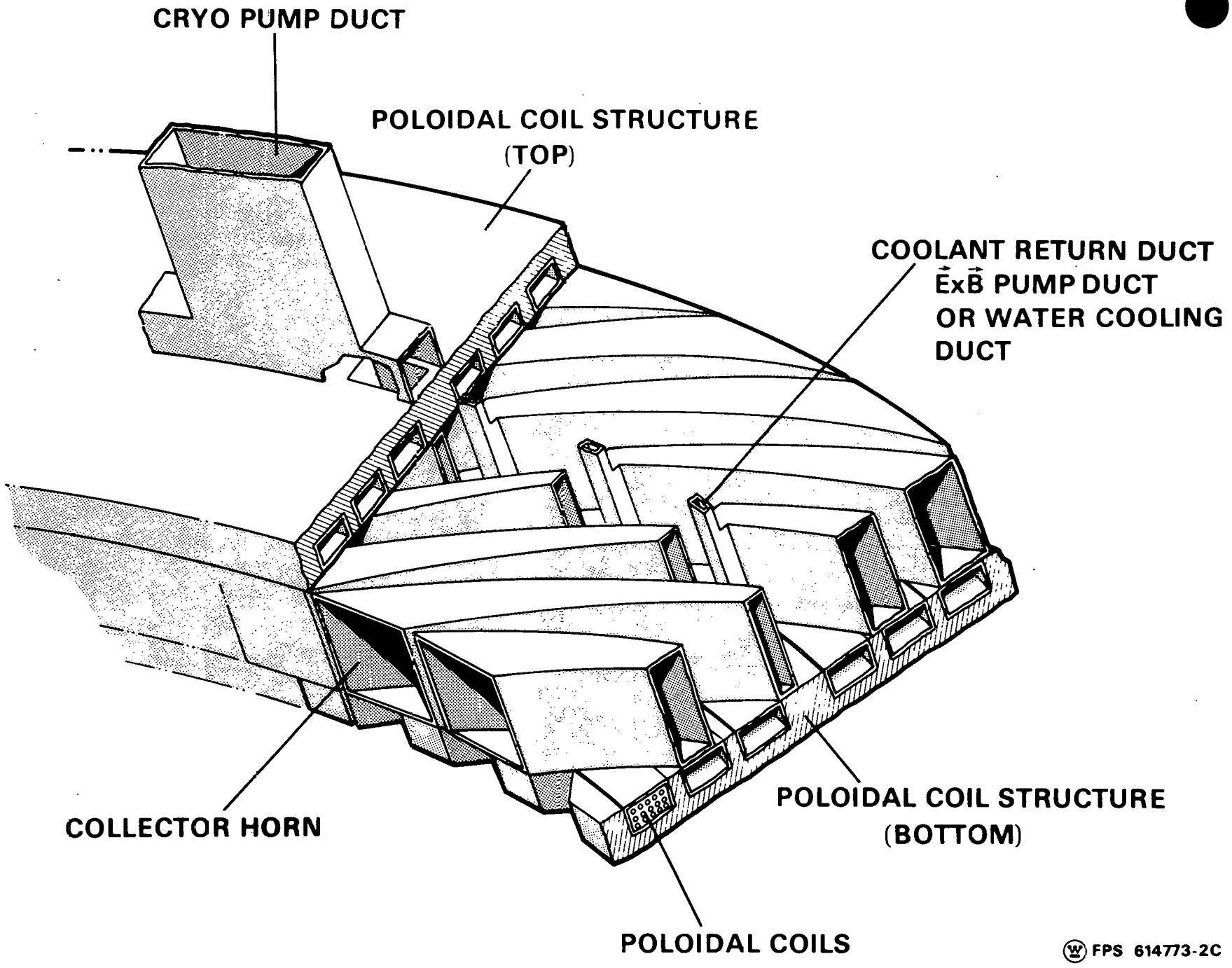

Figure 2-9. Trimetric view of the divertor assembly. The horn will house solid metal panels or will be lined with lithium wetted screens.

3.0 THERMAL DESIGN

In this section we discuss the thermal considerations associated with the use of liquid lithium films and the solid getters. The liquid lithium mass flow rate is estimated and the required circulating system is described. The reaction of the free surface lithium film in the strong magnetic field has not been examined in this study. The cooling method for the solid getter is described and the thermal characteristics of the gettering material are discussed.

3.1 THERMAL DESIGN FOR FLOWING LITHIUM

The total collecting surface area for the liquid lithium design described in Section 2.2 is about 320 m^2. For a total power deposition of 320 MW the surface heat flux is therefore 1.0 MW/m^2. The design temperature rise of the liquid lithium was selected to be 100°C, which is about 70% of the allowable temperature change of lithium from its melting point of 186°C and its boiling point of 325°C at the plasma vessel pressure of about 10^{-5} torr. With the above given heat flux and temperature rise, the total liquid lithium flow rate is:

$$\dot{m} = Q_T/C_p\ \Delta T = 320 \times 10^6/4.188 \times 100 = 764\ kg/sec \qquad (3\text{-}1)$$

where Q_T = total heat input = 320 MW
C_p = specific heat of lithium = 4.188 J/g °C
ΔT = lithium temperature rise = 100°C.

With this flow rate and the surface area, the film thickness of the liquid lithium fall was estimated to be about 0.2 cm which appears to be reasonable.

Since there are 192 wedge-shaped collectors in the design, the flow rate per collector is 764/192 = 4.0 kg/sec. Assuming one pipe is used to circulate the lithium flow per collector and the cross-sectional area of the pipe is 0.3 x .0333 = 0.01 m^2, the lithium flow velocity in the pipe is:

$$U_o = \frac{\dot{m}}{192\ A\rho} = \frac{4.0}{.01 \times 497} = 0.8\ \text{m/sec} \qquad (3\text{-}2)$$

where A = pipe flow area = .01 m^2
ρ = lithium density = 497 kg/m^3.

The Hartmann number for the lithium flow is[27]:

$$H_a = aB_\perp \sqrt{\frac{\sigma}{\eta}} \qquad (3\text{-}3)$$

where a = one-half of the width of the channel area = .01666 m
$B_\perp$ = transverse poloidal magnetic field = 4.5 tesla
σ = lithium conductivity = 2.22×10^6 mhos/m
η = lithium viscosity = 5.8×10^{-4} kg/sec-m.

Substituting the above values in H_a, one obtains

$$H_a = .0167 \times 4.5 \sqrt{\frac{2.22 \times 10^6}{5.8 \times 10^{-4}}} = 4638 \qquad (3\text{-}4)$$

The transition Reynolds number is[28]:

$$Re_t = 500\ H_a = 2.319 \times 10^6 \qquad (3\text{-}5)$$

whereas the Reynolds number of the flow is

$$R_e = \frac{\rho U_o a}{\eta} = \frac{497 \times 0.8 \times 0.017}{5.8 \times 10^{-4}} = 1.2 \times 10^4 \qquad (3\text{-}6)$$

which is smaller than the transition Reynolds number given in Eq. (3-5); therefore, the MHD Hartmann flow regime applies[28]. The calculations for the electromagnetic pump to circulate the lithium are described in Appendix A. The results of calculations are summarized in the following paragraphs.

The free surface lithium in the vacuum has to be recirculated by $\vec{E} \times \vec{B}$ pumps. The simplified geometry of the pump is shown in Figure 3-1. The dimensions are 2 w = 0.3 m, 2 a = 0.0333 m, and L = 1 m. The flow is along the Z-axis direction and the transverse magnetic field is along the X-axis direction. As shown in the last section, the Hartmann number of the flow is 4638, so that the flow is Hartmann and the flow velocity is given by the $\vec{E} \times \vec{B}$ drift or U_o = 0.8 m/sec.

The pressure gradient of Hartmann flow is given by the following equation:

$$\frac{\partial \vec{p}}{\partial Z} = \left\{ \frac{H_a^2}{R_e} \left[K - \frac{H_a}{H_a - \tanh H_a} \right] \pm \rho g L \right\} \hat{Z} \qquad (3\text{-}7)$$

where R_e is the Reynolds number and H_a the Hartmann number. In Eq. (3-7), $K = Ey/\bar{u} B_o$, where Ey is the electric field in y-direction, $\bar{u}$ is the average flow velocity, and B_o the magnetic induction. The second term of Eq. (3-7) is the pressure drop due to the magnetic viscosity. The third term is the gravitational pressure drop which is negligible in comparison with the magnetic pressure drop. The average velocity of the channel flow is given in the following expression:

$$\bar{u} = \frac{Ey}{KB_o} \qquad (3\text{-}8)$$

The factor $H_a/(H_a - \tanh H_a)$ is approximately 1 for large Hartmann numbers. Then K is chosen to be 1.1 to account for the pressure drop due to end effects, Hall effect, and nonuniformity of the magnetic field, which are neglected in Eq. (3-7). Making $\bar{u} = U_o$, the lithium mass flow velocity, and taking B_o = 4.5 T, the electric field required is:

$$Ey = K\bar{u} B_o = 3.96 \text{ volts/m.} \qquad (3\text{-}9)$$

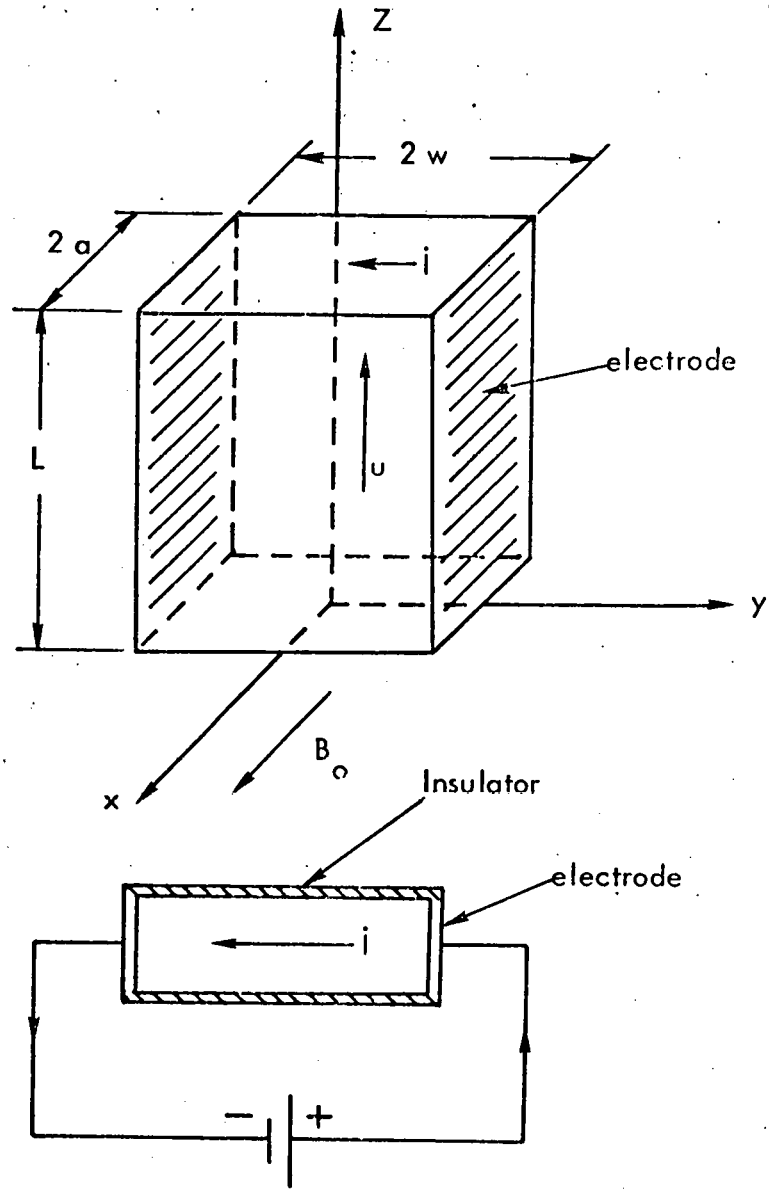

Figure 3-1. Simplified magnetohydrodynamic channel flow for the $\vec{E}$ X $\vec{B}$ pump.

The current per channel is

$$I = 2 (K - 1) \sigma B_o \bar{u} a = 27 \text{ kA/unit length} \quad (3\text{-}10)$$

The total power requirement is thus

$$W = 192 (I \cdot Ey \cdot 2 W) = 6.3 \text{ MW} \quad (3\text{-}11)$$

which appears reasonable.

If we use a current density in the leads of 1500 A/cm^2 for each pump, the cross-sectional area of the lead for each pump is 18 cm^2. The conductor size is quite significant. The joule heating in the conductor is

$$Q''' = J^2 \rho_{cu} = (1500)^2 (1.67 \times 10^{-6}) = 3.76 \text{ MW/m}^3. \quad (3\text{-}12)$$

Therefore, cooling of the conductor is necessary.

The above analysis shows that the electric field and power requirements are reasonable, but the conductor lead for supplying 27 kA of current to each pump is very heavy and requires a cross section of 4.3 cm x 4.3 cm with cooling. Since 384 such conductor leads are required, the system would be quite complicated. As a result, further theoretical work is required to improve this system.

3.2 THERMAL DESIGN FOR SOLID GETTERS

As discussed in Section 2.2, a surface with an area of 640 m^2 can be obtained and the thermal load can be designed to be as low as 0.5 MW/m^2, which makes the solid getter scheme attractive and competitive. The principle of solid getters is discussed in Section 5. Titanium has been chosen as the getter material in the present study because it has a high sticking probability (from 0.8 to 0.96), a saturation dose of 10^{18} cm^{-2}, and a sputtering yield of less than 1% at an optimum operating temperature range from -50 to 280°C. The cooling requirement for the titanium plates has been analyzed.

The getter plates and the horn housing walls are made of titanium double walls with pressurized water flowing in the space between the walls. The thickness of each wall is 0.3 cm and the gap spacing between the walls is 0.5 cm. It has also been assumed that only 85% of the plate surface area is available for cooling by water. Parametric transient heat conduction and hydraulic calculations were performed using the general purpose TAP-B code[29] to determine the plate and coolant temperatures along the plate cooling channel during a power deposition pulse. The results are shown in Figure 3-2. The power pulse profile used in the analysis is also shown in the figure. The profile consists of a linear power ramp from zero to 0.5 MW/m^2 in 10 seconds; a constant power deposition of 0.5 MW/m^2 for the next 10 seconds and then a linear down ramp to zero flux during the following 10 seconds. The profile is repeated in every cycle of operation. In the figure the plate surface temperatures at the beginning and at the end of the flat top portion of the pulse as a function of water flow rates are shown. It is seen from the figure that in order to keep the plate surface temperature below 280°C during a normal operating cycle, the water flow rate required is about 2.53 ℓps/plate. For six plates in each horn and 192 horns in the divertor, the total cooling water requirement is 2914 ℓps. At 2.53 ℓps/plate the maximum water temperature rise in the longest plate channel is about 25°C as shown by the bottom curve in the figure. The sudden change in slope of the plate temperature curves at 20 seconds is due to the transition from the turbulent to the laminar flow regime in the flow channel.

The temperature distribution across the getter wall thickness at the end of the power pulse flat top (at 20 seconds of the cycle) is shown in Figure 3-3. With this temperature distribution the resulting thermal stresses were calculated. The wall was assumed to have a boundary condition of fixed edges and the temperature gradient occurs only across the plate thickness. The in-plane thermal stress distribution is shown in the figure. The maximum stress is about 100 MPa which is below the maximum tensile stress of 138 MPa for the material.

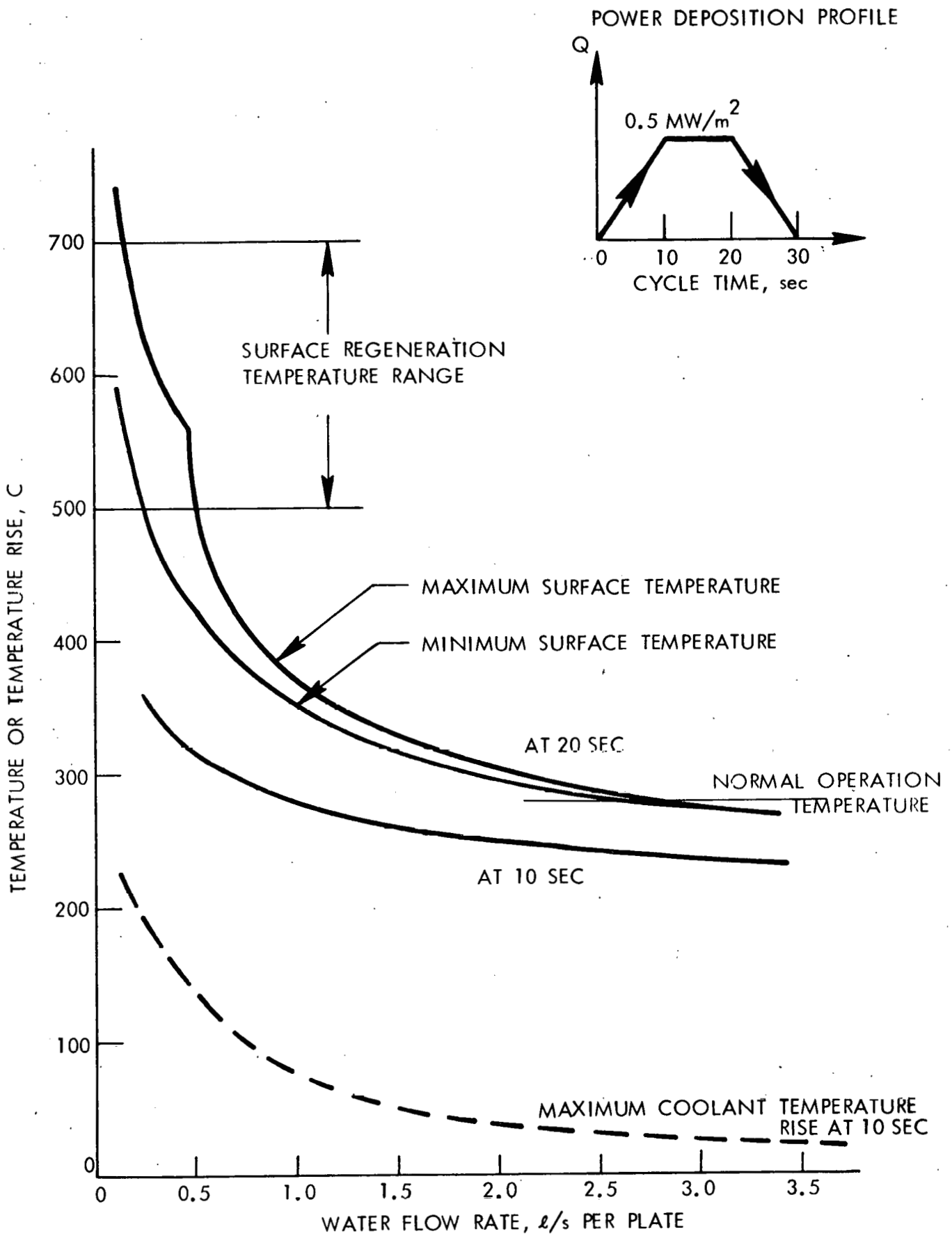

Figure 3-2. Getter plate surface temperatures and water temperature rise at different water flow rates.

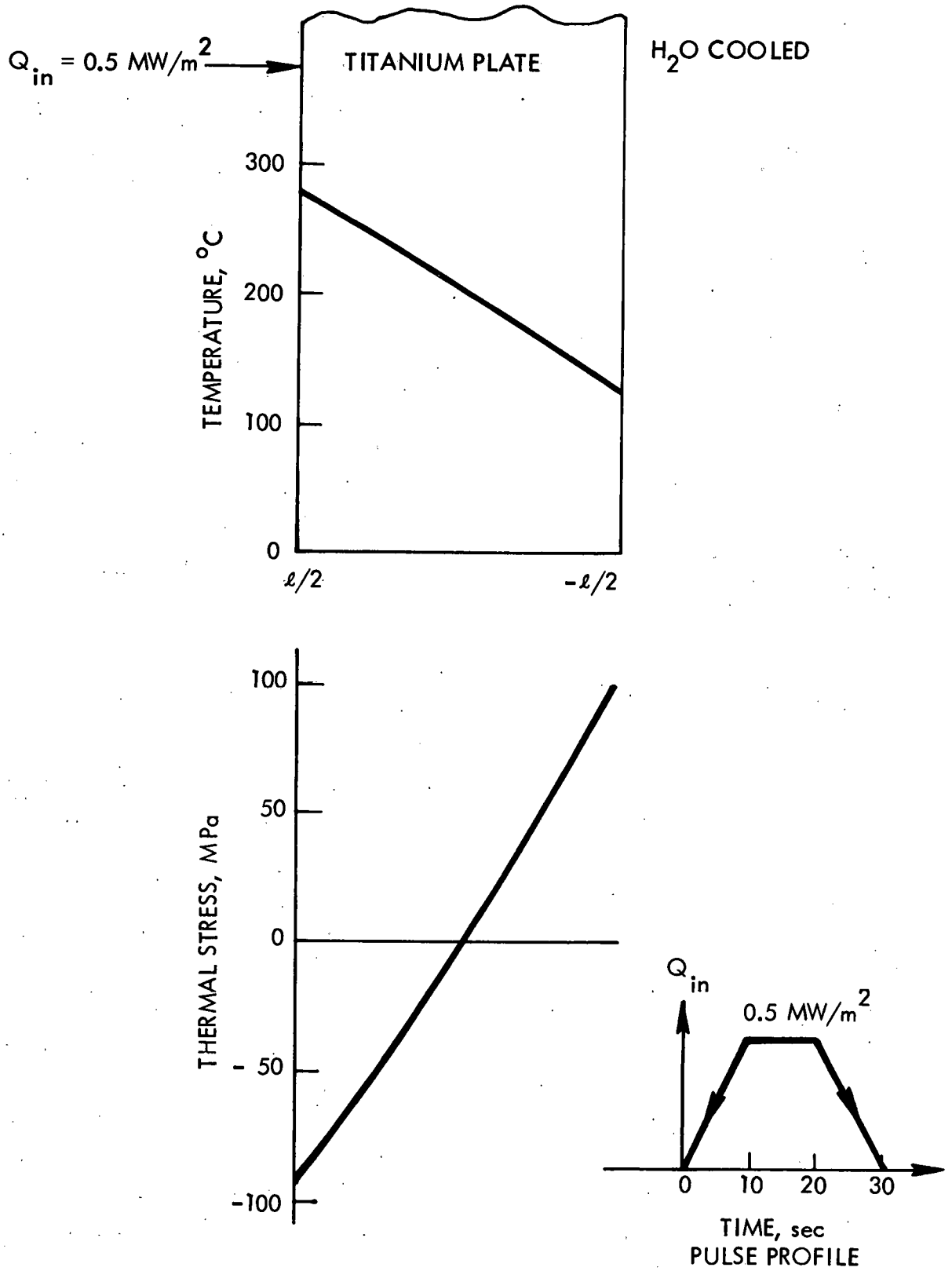

Figure 3-3. Temperature and thermal stress distributions at the end of a 10 second pulse.

For regeneration of the getter surface, an electrical heating system has to be designed. Another way to heat up the plate for regeneration is to reduce the cooling water flow rate during a pulse. As shown in Figure 3-2, if the regeneration temperature is between 500 to 700°C, the water flow rate can be reduced to about 0.2 ℓps/plate. With this reduced flow rate the maximum water temperature rise in the channel is about 170°C. A pressurized water system at about 10 to 11 atm is required. If this procedure of regeneration is found unsatisfactory, electric heaters can be installed at the back of the plates to heat the getters to any desired temperature for as long as required during the off cycle period for surface regeneration.

Without cooling, the peak adiabatic temperature of the plates with the same power deposition profile is 1135°C which is well below the melting temperature of the material. This indicates that in case of loss of coolant, the getters would still be intact for one cycle. The support structures would have to be designed to accommodate the resulting thermal motion.

As shown in Table 5-1 in the discussion of getter materials (Section 5.2.1), zirconium has a slightly higher sputtering yield of 3% (as compared to < 1% for titanium) but the optimum operating temperature range extends to about 390°C (as compared to 280°C for titanium). The cooling water required is therefore less than that for titanium plates. The trade-off is a 2% in sputtering yield between these two materials against the cooling water requirement. Titanium and Zirconium are hence two good candidates as solid getters for the divertor.

The thermal load in the leading edge of the solid plate due to particle impingement would be higher than the design value of 0.5 MW/m^2 on the plate side wall. If the leading edge surface is perpendicular to the particles path, the loading on the leading edge may be as high as 10 MW/m^2. By a careful design of the leading edge, however, the thermal load can be reduced to below 3 MW/m^2. One way is to round off the corner and to curve the leading edge into the horn interior so

as to increase the surface area. Another way is to bond a layer of material which has a high melting point and compatible coefficient of expansion, to the front end of the plate to protect the leading edge. Niobium and tungsten are good candidates for this application. Further study on this problem is required and planned.

4.0 MECHANICAL DESIGN

A conceptual mechanical design was developed to evaluate the engineering feasibility of the compact divertor concept. Our primary concern is whether or not we can provide the restraint to overcome the repulsive magnetic stress of about 10^6 newtons/m^2 between the pair of coil sets within the very much restricted space. It appears that this can be done with no difficulty. In the following subsections the method of designing the structure of the coil assembly and collection horns for both liquid lithium and solid getter approaches is discussed.

4.1 MECHANICAL DESIGN OF THE COIL ASSEMBLY

A workable design for the mechanical structure of the compact poloidal divertor and burial chamber concept for TNS is shown in Figure 4-1. The dimensions discussed here and shown on the associated figures are based on a point design of TNS-3 as the reactor model.

The main structure consists of two stainless steel dish-shaped, washer-like structures with an I.D. of 6.7 m and O.D. of 9.9 m. The dish-shaped structures are each approximately 19 cm thick and are separated by tubular spacers to form a gap of approximately 35 cm. This gap provides the burial chamber which, for the lithium case, houses the lithium-wetted screen lined collector horns, the lithium piping, and pumps. The dish-shaped structure is sloped 20° to the center of the reactor torus and is divided into 16 pie-cut segments to facilitate construction and assembly operations. Each segment has overlapping edges to provide circular continuity and to add structural strength at the intersecting joints. Cut into the inner face surface of each dish-shaped structure are six circumferentially oriented grooves for nesting the divertor coils. The three coil grooves on either side of the structure centerline are separated by a 20 cm wide rib while the adjacent coil grooves are separated by 5 cm wide ribs. The 20 cm rib at the center contains passageways for connecting the lithium piping network on the bottom structure to the top structure. The smaller adjacent ribs provide lithium passageways to the screens located inside the collector horns. In addition to the

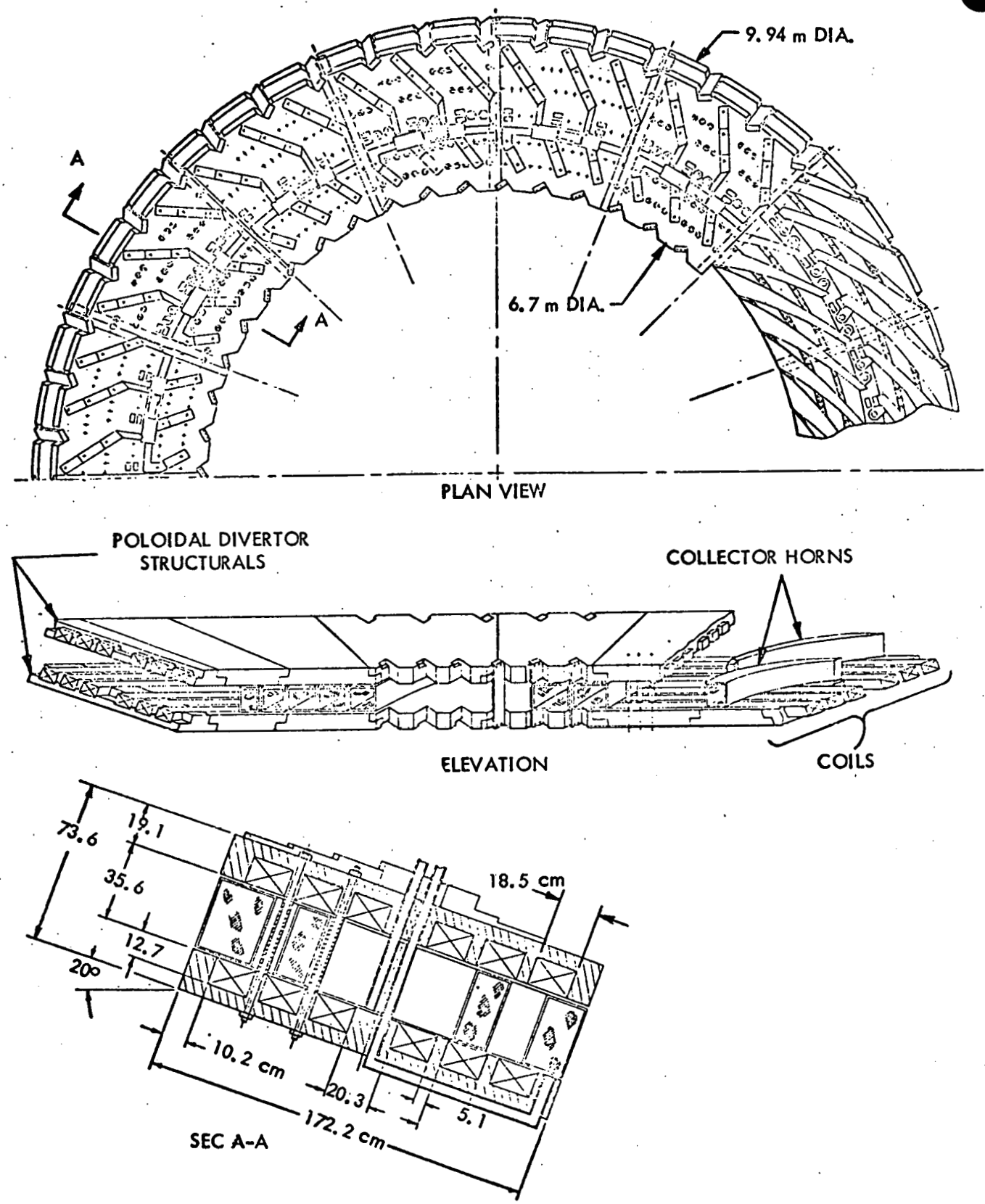

Figure 4-1. Plan and side view of poloidal divertor structure.

piping, the center rib and the three adjacent ribs on either side of the center rib contain the holes for the structural bolts which tie the upper and lower structure together. The top dish-shaped structure is spaced relative to the bottom dish-shaped structure by tubular spacers threaded over the structural bolts. These spacers provide the proper spacing (burial chamber) between the upper and lower set of coils while the structural bolts provide the restraint to overcome the total repulsive force between the two sets of coils. The design stress is 1.33×10^6 newton/m^2 which provides 30% margin.

The structural bolts are located in groups along the circumference of each rib such that they pass between the lithium-wetted screen lined collector horns. The outer and inner edges of the dish-shaped structure, as defined by the I.D. and O.D. of the structures, are held together by means of thin tension plates (1.6 cm) which are keyed and bolted to the top and bottom structures. These plates are notched into the circumference of the structure at such an angle as to align the thin edge of the tension plate with the collector horns. This provides the maximum entrance throat to the collector horns and minimizes the leading edge of the collector screen.

In a preliminary analysis of the top and bottom dish-shaped structure and the structural bolts, the cross section of the structure was treated as two separated and uniformly loaded continuous beams supported at seven points (see Figure 4-1). The first and last points corresponding to the outer and inner edges of the dish-shaped structure are supported by thin tension plates, while the five intermediate points are supported by structural bolts arranged in groups as required to meet the needed tensile loads.

One can calculate the bending moments over each support by using the theorem of three moments[30], expressed in the form

$$M_A L_1 + 2 M_B (L_1 + L_2) + M_C L_2 = \frac{W_1 L_1^3}{4} - \frac{W_2 L_2^3}{4} \qquad (4\text{-}1)$$

here M_A, M_B and M_C are the bending moments at the supports A, B, and C. L_1 and L_2 are the lengths between supports and $(\frac{-W_1 L_1^3}{4})$ and $(\frac{-W_2 L_2^3}{4})$ are the terms representing the particular loading on the beam. To simplify the calculations, Table 8 of reference 30 was used to determine the bending moments and loads at each support.

A maximum bending moment of 7.83×10^4 N·m and a maximum tensile load of 295×10^4 N occur at the mid-point of the structure and diminished to zero and 95.6×10^4 N, respectively, at the ends of the structure. To meet the load requirements, two 6.4 cm diameter bolts with a combined tensile stress area of 51.6 cm^2 is required at the mid-point and a tension plate with 24.2 cm^2 cross-sectional area is required at the ends of the structure. The two supports on either side of the mid-point is provided by two groups of bolts. Each group contains three 4.8 cm diameter bolts with a total tensile stress area of 42.4 cm^2 for each group.

4.2 MECHANICAL DESIGN FOR FLOWING LITHIUM

A piping manifold is attached to the top surface of the upper dish-shaped structure to provide distribution of the liquid lithium to the surfaces of the screens mounted inside the collector horns. To help reduce the heat load on the lithium as it passes over the screens, the lithium is introduced onto the screen at three places along the length of the horn. Each liquid lithium inlet is located approximately 1/3 distance along the path of the lithium as it flows over the screen. If the liquid lithium were to enter one end of the collector horn at T_i and exit the other end at T_o, it would increase in temperature by some ΔT; however, with liquid lithium being introduced at two more points along the path as proposed in this design, the temperature rise of the liquid lithium is reduced by the intermixing of liquid lithium at a temperature T_o from the additional inlets.

The assembled dish-shaped structure is mounted inside, near the top of the vacuum vessel and supported by tension members which transfer the load through the vacuum vessel to the external reactor structures. A similar assembly is installed inside,

near the bottom of the vacuum vessel and is supported from the floor of the reactor base by compression members that transmit the loads through the vacuum vessel.

The getter system for this concept consists of liquid lithium-wetted screen lined collector horns, 96 inside and 96 outside types, as shown in Figure 4-2. The throat opening of the collector horns mounted on the inside circumference of the dish-shaped structure is 43.9 cm wide while those mounted on the outside circumference of the structure have a throat opening of 65.1 cm. Both types of collector horns are 35.5 cm high.

The collector horns are constructed of heavy gage stainless steel (0.5 cm) and the inner surfaces are lined with metal screening. The screening on the top and sides of the horns are designed to have a clearance between the screen and the internal surface of the horn such that the screens can be totally engulfed with liquid lithium. The clearance between the bottom screens and the bottom of the horn is achieved by having the screen rest on several ribs attached to the inner surface of the horn bottom plate. The top plate of the horn is recessed and contains many small holes to provide distribution of the liquid lithium on the top and side screens. The small holes are eliminated in the horn top plate just below the three liquid lithium inlet ports to prevent the lithium from passing on through the screen. The lithium that travels down the side screens is collected on the bottom plate of the collector horn. Coverage of the bottom screen with liquid lithium is assured by the small metal ribs or divider plates which are constructed across the bottom plate of the horn. As the liquid lithium spills over the divider plates it will come in contact with the bottom screen; because of the good wetting characteristics of the liquid lithium it will travel along the surface of the bottom screen.

Once the lithium has traveled to the narrow end of the outside collector horn it will drain off into a reservoir where it will be pumped out of the horn by electromagnetic $\vec{E} \times \vec{B}$ pumps and out of the vacuum vessel by supplementary pumping systems to a point where the lithium will be cooled and reconditioned for a return cycle.

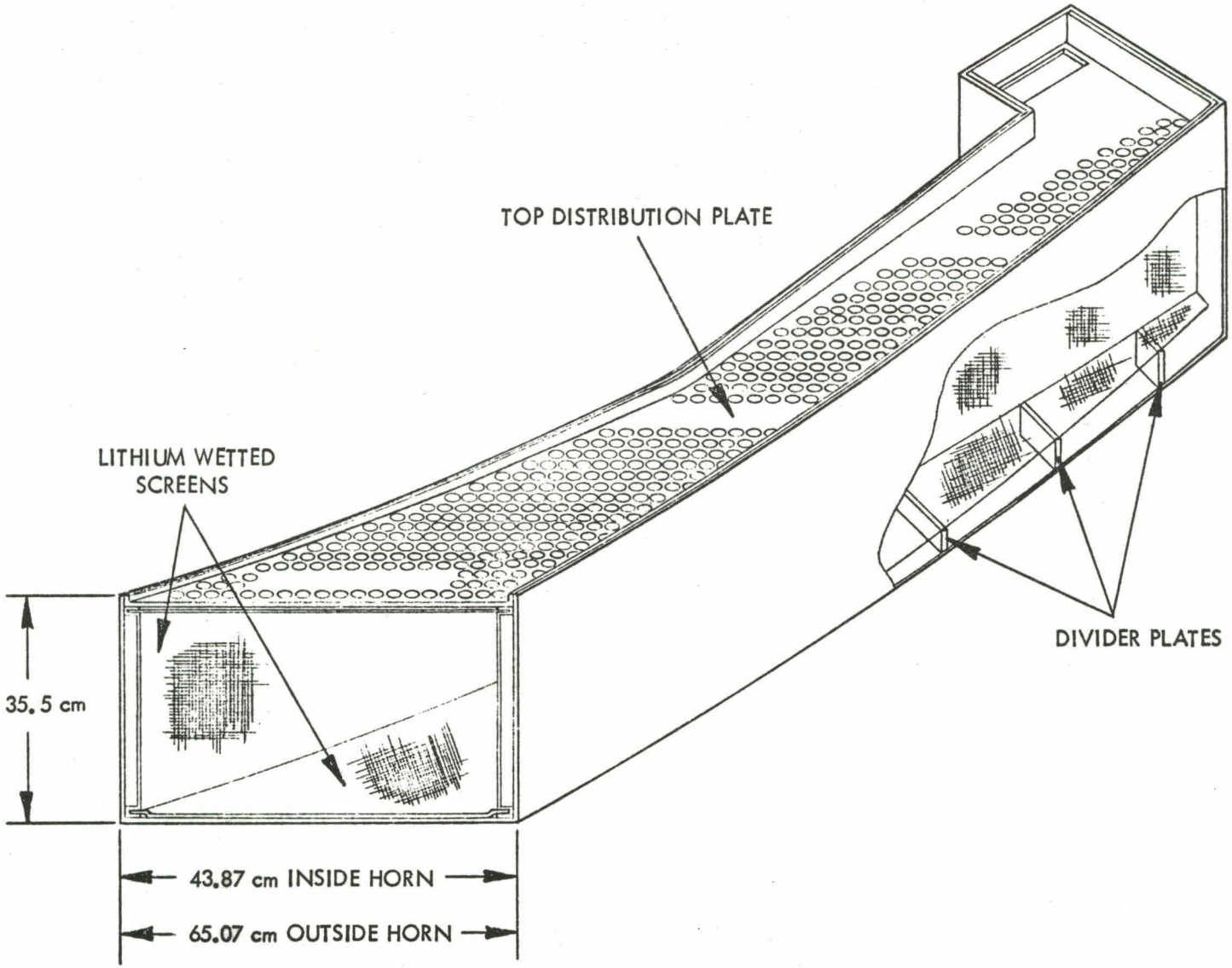

Figure 4-2. Collector horn with liquid lithium-wetted screens.

The inside collector horns are similar in construction but in this case the liquid lithium is introduced into the collector horn from the small end and allowed to run down the screen to the large end where it is also removed by the $\vec{E} \times \vec{B}$ pumps and recycled in the same manner as the liquid lithium from the outside collecting horns.

4.3 MECHANICAL DESIGN FOR SOLID GETTERS

The design of the structural members of the compact poloidal divertor is such that the liquid lithium-wetted screens enclosed in the collector horns can be replaced with a solid collecting target as shown in Figure 4-3. The physical dimensions of the collector horn and the method of attaching the collector horn remain unchanged. The solid getter horn design uses a double wall construction technique for cooling and is made of titanium. The horn consists of a top and bottom panel, one full length vertical inside curved panel and short length back panel. Six intermediate panels of varying length are spaced evenly inside the horn. The intermediate panels are installed to increase the surface area needed to reduce the heat and particle flux loads. The back side of the intermediate panels contain fins that run from top to bottom of each panel. These fins serve as traps for neutral particles. The back vertical panel of the horn does not extend the full length of the getter horn to allow any neutral particles that are not trapped by the fins on the back side of the panels to pass through the horn and collect on additional panels of Zr/Al which are located between adjacent horns.

Each panel of the solid getter horn is approximately 1.1 cm thick with a 0.5 cm void between plates for the water coolant. The cooling water is fed into the top panel of the getter horn at the large end and is removed from the bottom panel at the narrow end. A side view of this design is again shown by Figure 4-4.

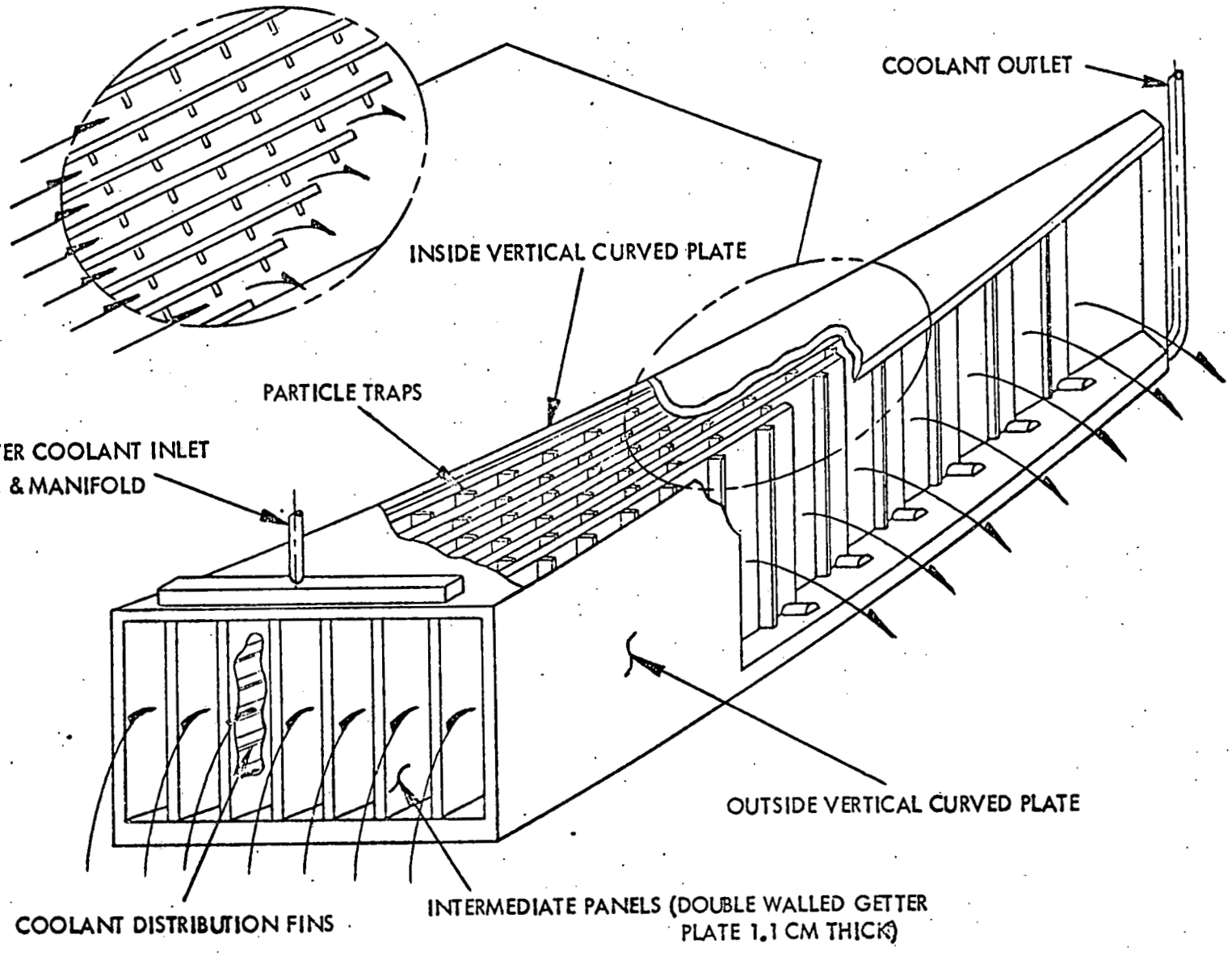

Figure 4-3. Collector horn with intermediate panels.

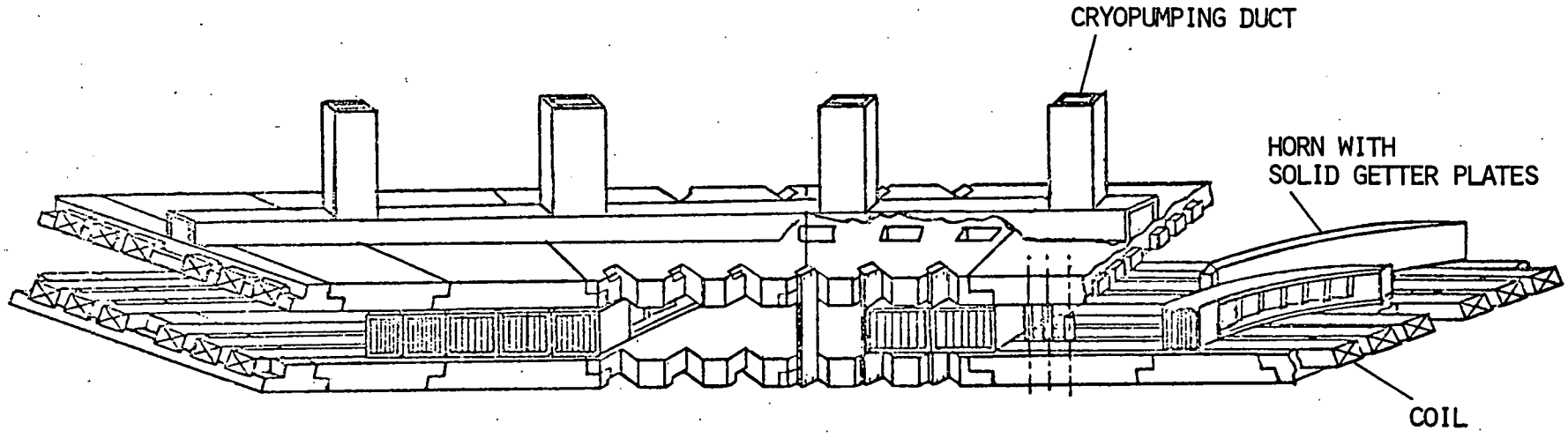

Figure 4-4. Side sectional view of compact poloidal divertor with solid getters.

5.0 VACUUM CONSIDERATIONS

To maintain the pressure in the divertor burial chamber below 10^{-5} torr, auxiliary pumps are needed to remove the residue neutral hydrogen molecules and helium. The pumping requirements for both collecting methods, liquid lithium and solid getters, are discussed in the following subsections.

5.1 LIQUID LITHIUM SYSTEM

The sorption coefficient of hydrogen isotopes by liquid lithium has been measured to be 95% experimentally[25]. It has been shown that a hydrogen molecule sorption coefficient of 99.9% can be achieved with the lithium screen arranged like chevrons[23]. However, the sorption coefficient of helium is zero, therefore, auxiliary pumping is necessary. For simplicity, the optimistic assumption will be made that the lithium trapping efficiency for hydrogen isotopes is 100%. The alpha concentration is approximately 2% of the total number of particles diffusing from the plasma. Since the throughput of charged particles to the divertor is equivalent to 1500 torr liter/sec, the throughput of the helium to the auxiliary pump is 30 torr liter/sec. This results in a pumping speed requirement of 3×10^6 liter/sec for an operating pressure of 10^{-5} torr. Using a helium pumping speed of 3.7 liter/sec cm^2 for a cryosorption panel, a pumping surface of 81.0 m^2 of cryopanel is required to handle such a throughput. This area requirement is too high unless higher operating pressure is allowed.

5.2 SOLID GETTER SYSTEM

It appears, from the previous analysis, that the flowing liquid lithium system is complicated and contains unknown physical uncertainties. The pumping requirement for helium alone is too high to handle, even with the most optimistic assumptions. The fact that the removal of helium is one of the main purposes of the divertor led to a serious look at the use of solid metal getters.

The principle and methods of using solid getters to achieve an ultrahigh vacuum are well-known[31,32] and such getters are commercially available. Their application to the fusion reactor has been discussed by several authors[25,33-35]. However, the use of solid getters to collect particles in the divertor burial chamber has not been seriously investigated. We have performed a detailed investigation to understand the problems in order to demonstrate whether or not such a method is feasible. The evaluation given here, based on the presently available data and information, has shown that the solid getters are indeed very promising and relatively simple with our particular divertor concept. In the following, the physical properties of the materials suitable for getters, the particle collection scheme, and overall vacuum considerations are discussed[36].

5.2.1 Survey of Getter Materials

The principle of ion pumping and the applications in ultrahigh vacuum have been discussed in detail by Redhead, et al.[31], and others. The mechanisms involved are entrapment, penetration, and channeling. In fact, the entrapment in solids of positive ions is the only mechanism for gettering rare gases such as helium. The trapping coefficient ranges from 0.0 to 0.96% depending on the incident ion, its energy, target material, and its temperature. The thermal reemission rate is generally low and for constant temperature is given by[31]:

$$F_r(t) = \frac{nk}{t} \text{ molecules/sec} \qquad (5\text{-}1)$$

where n is the number of molecules trapped at time zero, t = 0, and k is the reemission constant; k was found to be proportional to (1-s) where s is the sticking probability[31].

For the thermonuclear application the problem is more difficult. The divertor pumping system must be capable of maintaining a high vacuum while handling a large flux of very energetic particles diverted from the scrape-off zone of the plasma. Thus, the collector must have the capacity for both the particle and

thermal loads. What is desired is a high sticking probability, a low sputtering yield, and at the same time, the capacity for gettering large numbers of particles (hydrogen and helium). The other physical characteristics which are of interest are the melting point, the density, and thermal stress. The metals with high melting points investigated for this gettering application are surveyed and tabulated in Table 5-1. The early data is mostly for the heavy rare gas ions[31]. Recently, more experimental information has become available for helium and deuterium ions[37-40] which include little data on the effect of the target temperature in the range of interest here. Therefore, some of the values in Table 5-1 represent our extrapolation of the published data. The sputtering yields are extrapolated from references 41 through 44. In Table 5-1 the temperature range given represents the range in which the sticking probability is greater than 0.8. The typical behavior is shown in Figure 5-1. The curves in this figure show flat-tops with sticking probabilities greater than 0.9; these values are listed as the maximum values in Table 5-1. The sticking probability of 0.8 is the value at the high end of the temperature range in Table 5-1. The ion energies range from 1 to 15 keV. The capacity of the getter materials is defined as the dose before saturation occurs. The typical dependence of saturation on ion energy is shown by Figure 5-2. The saturation dose, as well as the capacity, increases with incident ion energy. Of the metals listed in the table, the data for titanium are the most up-to-date and complete and offers the best characteristics. It has a wide and suitable temperature range, high sticking probability, high saturation dose, and low sputtering yield.

As mentioned above, the only mechanism for pumping rare gas, e.g., helium, is the entrapment of the ions in the solid metal. Helium produced in the thermonuclear reaction is diverted from the plasma together with other ions; principally, hydrogen isotopes. In the present scheme, the hydrogen ions are pumped principally by impact and diffusion in the titanium while auxiliary pumping must be provided for the helium. Although the area available for auxiliary pumps is limited, and only limited pumping speed can be obtained, the maximum concentration of helium

TABLE 5-1

COMPARISON OF IMPORTANT THERMOPHYSICAL PROPERTIES OF SOLID GETTER MATERIALS

(1) Sticking Probabilities for a Given Target Temperature Range. The Lower Sticking Probabilities are the Values at the Low and High Ends of the Temperature Range.

(2) Saturation Doses and Sputtering Yields for Several Metals are for H^+ or D^+ at Normal Incident Energy Ranging from 1 to 5 keV

Element	Melting Point °C	Density g/cm^3	Atomic Weight g	Optimal Temperature Range °C	(1) Sticking Probability		(2) Saturation Dose cm^{-2}	Reemission Constant k	(2) Sputtering Yield %
					lower	max			
Er	1400	9.16	167.3	160-650	0.8	0.92	-	-	3.0
Mo	2620	10.20	95.94	-	0.8	-	$\sim 10^{17}$	4.3×10^{-3}	-
Nb	2415	8.57	92.90	(-70)-230	0.8	0.96	2×10^{17}	-	< 0.9
Ta	2996	16.60	180.95	-	0.9	-	10^{18}	-	-
Ti	1725	4.50	47.90	(-50)-280	0.8	0.96	10^{18}	-	< 1.0
W	3410	19.40	183.85	-	0.8	-	5×10^{16}	-	-
Zr	1857	6.49	91.22	(-10)-390	0.8	0.96	10^{18}	-	3.0

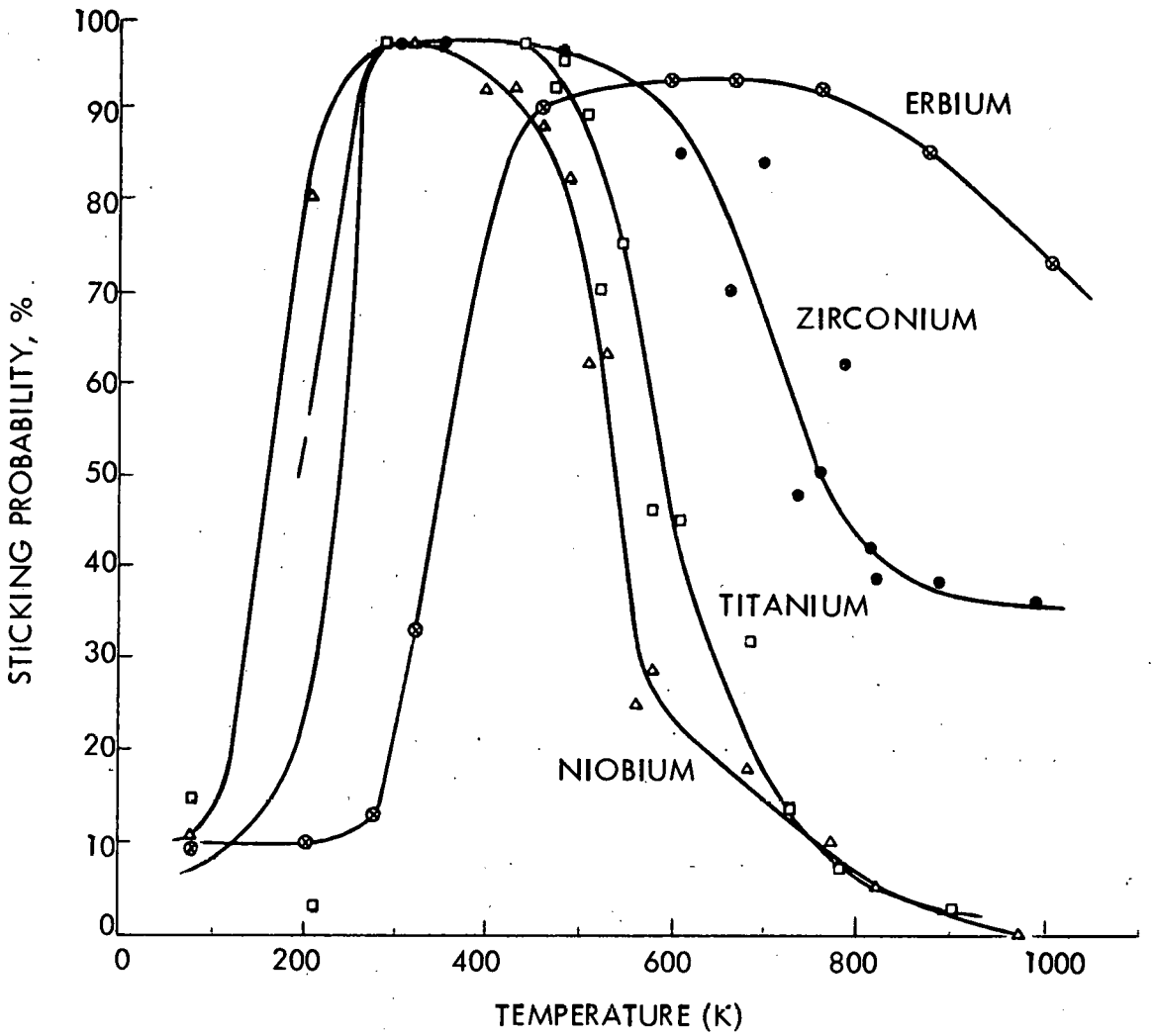

Figure 5-1. Temperature dependence of the sticking probabilities of D^+ ions in Niobium, Titanium, Zirconium, and Erbium. The maximum sticking probabilities are as high as 96%. Over a wide temperature range the sticking probability is > 80%. (McCracken and Jefferies, ref 40)

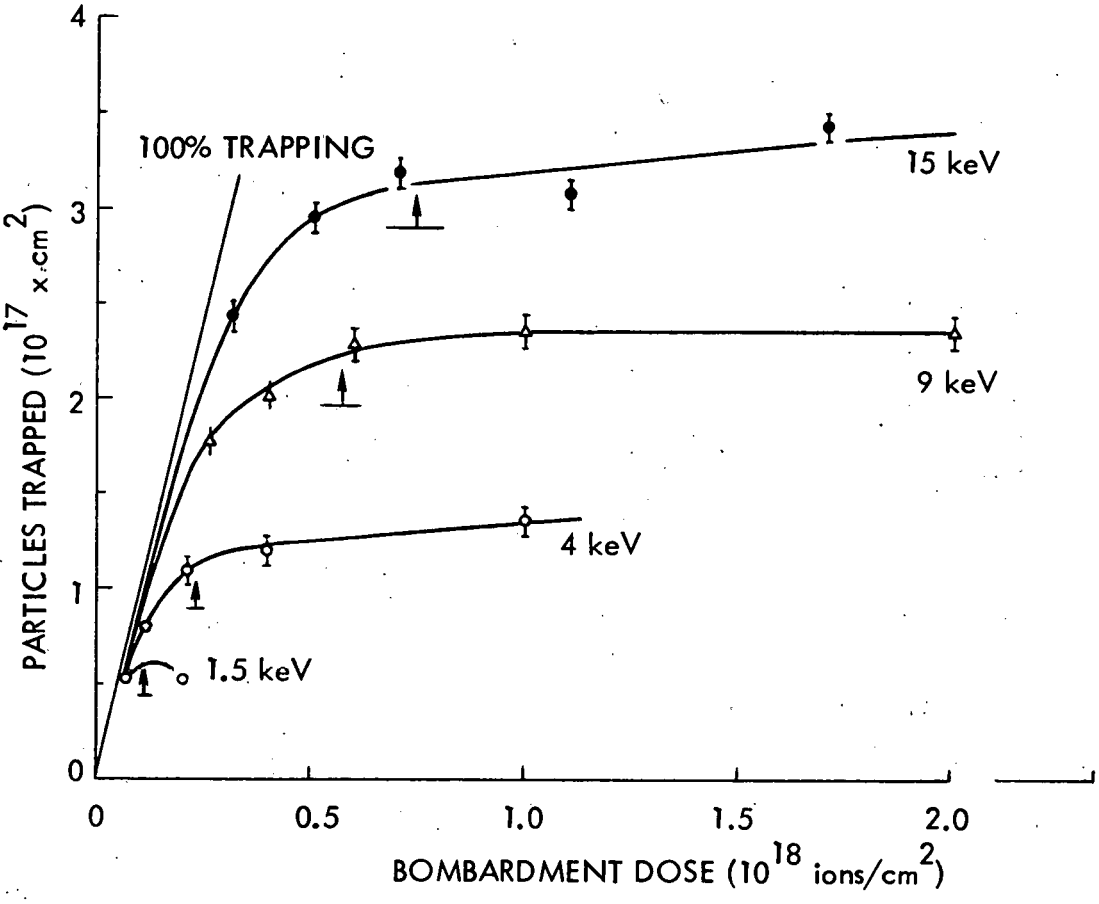

Figure 5-2. Saturation curves of the trapping of ^{3}He ions in a Niobium single crystal for different energies implanted to different doses in a random direction. The trapping efficiency ~ 100% at dose of < 10^{17}/cm^2 at 1.5 keV. (Behrisch, et al. ref 39)

will be $\sim 2\%$; therefore, a relatively low pumping speed for helium is required. We will return to the auxiliary pumping speed determination after consideration of the pumping and backstreaming of the principal gas, hydrogen.

5.2.2 Hydrogen and Helium Pumping and Backstreaming

Hydrogen ions enter the burial chamber of the divertor directed by the magnetic field lines, and enter the narrow titanium channels. As shown in Figures 2-7 and 4-3, these channels are finned to increase the trapping efficiency. After the first impact we assume the ions to be neutralized and the hydrogen to be in the molecular state. The trapping efficiency of such a long channel has been studied in detail by Sucov[23] using numerical integration where spatial distributions of the incident and scattered particles have been properly taken into account. A 99% trapping efficiency has been predicted. For the purpose of demonstrating the feasibility of the present scheme, we will use a simplified approach which will give a conservative estimate of the hydrogen pumping efficiency and backstreaming[36].

We denote the sticking coefficient for ions (H^+, D^+, or T^+) to be s_1 and that for neutrals (H_2, D_2, DT, etc.), s_o. Then the escape coefficients, e_1 and e_o are:

$$e_1 = 1 - s_1 \tag{5-2}$$

$$e_o = 1 - s_o \tag{5-3}$$

for ions and neutrals, respectively. The overall trapping coefficient after n collisions, or "bounces," at the titanium surfaces is given by the geometric series

$$s = s_1 + e_1 \sum_{i=1}^{n} e_o^{\,i-1} s_o \,, \tag{5-4}$$

the sum of which is well-known, enabling us to write

$$s = s_1 + e_1 s_o \frac{1 - e_o^n}{1 - e_o} = s_1 + e_1 (1 - e_o^n). \tag{5-5}$$

The limits with respect to n are trivial but interesting; for n = 0, i.e., a "channel" of infinitessimal length, $s = s_1$, while for $n = \infty$, i.e., an infinitely long channel, s = 1. Assuming the fins on the titanium channel walls to have a height to separation distance ratio of ~ 5, we assume s_o to be ≈ 0.1[35]. For hydrogen ions having an energy ~ 3 keV, as expected for the diverted ions, s_1 can be taken to be ≈ 0.8. Thus, after only a few bounces the overall trapping efficiency approaches unity; for the assumed s_1 and s_o we obtain after only "six" bounces, s = 0.9. Since the channels are relatively long, narrow, and lined with fins; and since the energetic ions enter nearly axially, the neutrals can be expected to be required to make many collisions, on the average, with the titanium before escaping either at the entrance or exit end of the channel. Thus, s = 0.9 is a conservative value.

The fraction of the neutrals that escape at the channel entrance is of concern because these particles provide a cold gas influx to the plasma. At the exit end of the channels a good hydrogen getter, e.g., Zr/16% Al, is provided to capture untrapped neutral hydrogen isotopes. Particles emerging from the channels will either be captured by the getter, whose speed is S_G, by an auxiliary pump of speed S_A, or they will reenter the channels. We are interested in determining the fraction of the particles diverted into the titanium channels that can reemerge from the channels; this amounts to the backstreaming ratio and is given by the product of the probability of transmission through the channels, 1 - s, the probability of not being captured by the getters or auxiliary pump at the exit end of the channels, $A_{ch}\, C_o/(A_{ch}\, C_o + S_G + S_A)$, and the probability of transmission back through the titanium channels, $1 - (s - s_1)$. Here, A_{ch} is the cross-sectional area of the channels and C_o is the conductance of an orifice of unit area. Then the hydrogen backstreaming ratio, F_H, is given by

$$F_H = (1 - s)\, A_{ch}\, C_o\, (A_{ch}\, C_o + S_G + S_A)^{-1}\, (1 - s + s_1). \qquad (5\text{-}6)$$

For convenience we will consider the diverted gas to be deuterium and use the same values of s and s_1 as above. The cross-sectional area of the channels can be made

to approximate the total area of the divertor throat; which, for a device of dimensions anticipated for TNS, is approximately 20 m^2. Using C_o for deuterium, 31.3 liter/sec cm^2, and a pumping speed of 2 x 10^6 liter/sec by the Zr/Al getters (corresponding to a projected area of some 35 m^2 of appropriately corrugated getter strip) and no auxiliary pumping, the resulting backstreaming ratio is $\approx$ 0.07.

$$F_H = (1 - 0.9)\ (20 \times 10^4 \times 31)\ (20 \times 10^4 \times 31 + 2 \times 10^6)^{-1} \times (1 - 0.9 + 0.8), \quad (5\text{-}7)$$

and

$$F_H \simeq 7\%$$

As stated above, auxiliary pumping must be provided for the helium since it is not gettered by either the Zr/Al, except by ion burial at its first impingement, or by the titanium. To determine the auxiliary pumping speed required, we can expect some 60% of the helium ions to be embedded in the metals listed in Table 5-1 up to a concentration on the order of 10^{17} atoms/cm^2, i.e., $s_I = 0.6$[31].

As is shown in Figure 4-4, we assumed that the auxiliary pump, i.e., the cryopanels in this case, were at the top center of the divertor assembly and in the gap between TF coils. This system was used as a model to analyze pumping requirements as a reference for future designs. The geometry was simplified by pessimistically assuming that most of the helium ions strike near the front end of the panels. Some fraction of the escaped neutral heliums will travel through the titanium channel of average length L and the Zr/Al channel of average length ℓ and enter the cryopanel duct. The overall free molecular conductance of the Ti and Zr/Al channels in series is approximately $C_{L+\ell}$ = 1.6 x 10^4 ℓ/sec for the dimensions used in the present conceptual design. The helium backstreaming ratio, F_{He}, is then approximately given by:

$$F_{He} = (1 - s_I)\ \frac{1}{A_{ch}\ C_o + C_{L+\ell}}\ \left\{ A_{ch}\ C_o + \frac{(C_{L+\ell})^2}{S_A + C_{L+\ell}} \right\}. \quad (5\text{-}8)$$

This equation correctly predicts the maximum backstreaming ratio which is $(1 - S_I) = 0.4$ when $S_A = 0$. The minimum backstreaming ratio which we can obtain is 0.16 for $S \to \infty$. For $S_A = 6 \times 10^3$ ℓ/sec per horn, the backstreaming ratio is approximately 0.2. This implies that a total of 32 m^2 of cryopanel surface is needed, by using a specific speed for helium of 3.7 liter/sec cm^2 for a 4.2 K cryosorption panel[45]. The requirement is still high and indicates that further optimization of the system is necessary.

Another important quantity is the gettering capacity which can be estimated from the saturation doses from the available data as listed in Table 5-1. The particle leakage rate of the reference plasma is approximately 5×10^{22} particles/sec[2]. The particle flux impinging on the particle collecting surface is

$$\Gamma = 7.8 \times 10^{19}/m^2 \text{ sec.}$$

The saturation dose for hydrogen in a Ti getter is $10^{22}/m^2$. For a burn time of 10 seconds the panel will reach saturation in approximately 13 pulses, i.e., the panel must be reactivated every 13 pulses, or about once an hour at design conditions.

The operating pressure for this solid getter system can be estimated as follows: from Table 2-1 the throughput to the divertor system is approximately 1500 torr liter/sec; the partial pressure of hydrogen molecules is

$$P_{H_2} = \frac{1}{2}\left(\frac{0.98\, Q_p\,(1 - s)}{S_{Zr/Al} + S_{cryo}}\right) = \frac{1}{2}\left(\frac{147}{2 \times 10^6 + 3.2 \times 10^6}\right)$$

$$= 1.4 \times 10^{-5} \text{ torr ;}$$

and the helium concentration is about 2% of the total diverted particles; the partial pressure of helium is

$$P_{He} = \frac{Q_p \times 0.02 \times (1 - S_1)}{S_{cryo}} = \frac{12}{1.0 \times 10^6} \cong 1.2 \times 10^{-5} \text{ torr;}$$

therefore, the total operation pressure is

$$P \cong 2.6 \times 10^{-5} \text{ torr.}$$

5.2.3 The Erosion Problem

The sputtering coefficient for titanium given in Table 5-1 is $\varepsilon = 0.01$, then the erosion rate would be

$$\dot{n}_s = \Gamma \cdot \varepsilon = 7.8 \times 10^{19} \times 10^{-2} = 7.8 \times 10^{17} \text{ atoms/m}^2 \text{ sec.}$$

The lifetime of the panel can be estimated from

$$\tau = \left(\frac{\rho}{m} N_o \delta\right)/\dot{n},$$

where m is the molecular weight, N_o is the Avogadro number, ρ is the density, and δ is the thickness of the panel that is permitted to be sputtered away. Assuming δ = 1 mm, we have

$$\tau = \left(\frac{4.50}{47.9} \; 6.023 \times 10^{23} \times 10^{-1}\right)/7.8 \times 10^{13}$$

$$= 7.3 \times 10^{7} \text{ sec}$$

$$\cong \frac{7.3 \times 10^{7}}{24 \times 3600}$$

$$= 845 \text{ days .}$$

This is about 2.3 years and assumes continuous operation of the divertor, i.e., a duty cycle of 100%. For TNS and a duty cycle of 10% this panel lifetime would be 23 years.

6.0 THE COMPARISON OF THE COLLECTOR METHODS

The features of liquid lithium film and solid titanium metal getters are compared as shown in Table 6-1. Lithium has the advantage of being continuously renewable; therefore, it can tolerate higher power densities and particle flux and thus is more suitable for steady state operation. However, the lithium circulating system is complicated and the helium pumping is difficult. The principal advantage of the solid getter is that it has a greater than 60% trapping efficiency for H_e^+ ions and it has a very high trapping efficiency for hydrogen isotope ions. Therefore, the auxiliary pumping requirement is much reduced and more manageable. The system is also simplified. However, the gettering capacity is low and the system has to be periodically reactivated.

TABLE 6-1

MAJOR DESIGN FEATURES FOR LIQUID LITHIUM AND SOLID TITANIUM GETTERS

	Lithium	Titanium
Collecting Surface Area	320 m^2	640 m^2
Thermal Load	1 MW/m^2	1/2 MW/m^2
Temperature	200-300°C	20-280°C
Cooling Method	Recirculated by $\vec{E}$ X $\vec{B}$ Pumps	Water Cooled
Pumping Requirement	E = 3.6 V/m/Pump I = 27 kA/Pump 1 Pump/Horn Power = 6 MW Total	Total Water Flow Rate = 2914 liter/sec
Number of Horns	192	192 6 Ti Panels/Horn
Helium Gettering Efficiency	~ 0	~ 0.6
Lifetime	Continuously Renewable	~ 23 Years With 1 mm Thickness of Ti
Particle Capacity	Limited by the Mass Flow Rate	Limited by the Saturation Dose
Tritium Recovery	Reprocessing Technology is not known and may be difficult	Released by Heating to High Temperature
MHD Effect	The Characteristics of Flowing Lithium Film in the Magnetic Field are not known	No Effect

7.0 IMPACT ON TNS SIZE AND ECONOMY

A sectional trimetric of the divertor assembly is shown in Figure 2-9. The cross-sectional view and a sectional trimetric of the overall compact poloidal divertor concept implemented for a particular TNS-4 reactor is shown in Figure 7-1 and 7-2. This particular version of TNS employs superconducting Nb_3Sn TF coils. Earlier discussions (Section 2) have dealt with TNS-3 which uses superconducting NbTi TF coils. TNS-4 is somewhat more amenable to the inclusion of this divertor concept than is TNS-3, in fact, the divertor is accommodated within the clearances already existing in the particular point design examined. Regardless of which coil technology is chosen, it appears that the compact divertor discussed in this text can be implemented with minimal impact on overall machine size.

The dotted areas in Figure 7-2 indicates the location of shielding provided to protect the TF coils against direct and scattered neutrons and gamma rays. The broken lines indicate the approximate boundaries of the fully developed D-shaped plasma. The arrowed lines with spirals suggest the motion of diverted charged particles entering the collector horns. Detailed neutron transport calculations have not been performed for this geometry; however, it appears possible to provide sufficient neutron shielding in the space available.

The divertor currents, except the equilibrium maintaining current I_{EF-D}, are proportional to the toroidal field strength; thus, they can be run at steady state similar to the TF coils. Whether larger or smaller currents are required for this particular divertor design is not conclusive unless specific designs for the other methods are made for comparison. However, the values of the divertor currents are very reasonable.

Our preliminary evaluation indicates that this divertor adds less than 10% of the total TNS cost which includes hardware, tritium handling, and the cooling system for handling additional ohmic heating in the divertor coils if copper is assumed. No additional cooling system is required for the thermal load to the divertor because the same amount of thermal power will go to the liner or first wall without a divertor. Due to the same reason, the cooling system of the liner or first wall will be much simplified and is reduced in cost when the divertor is used.

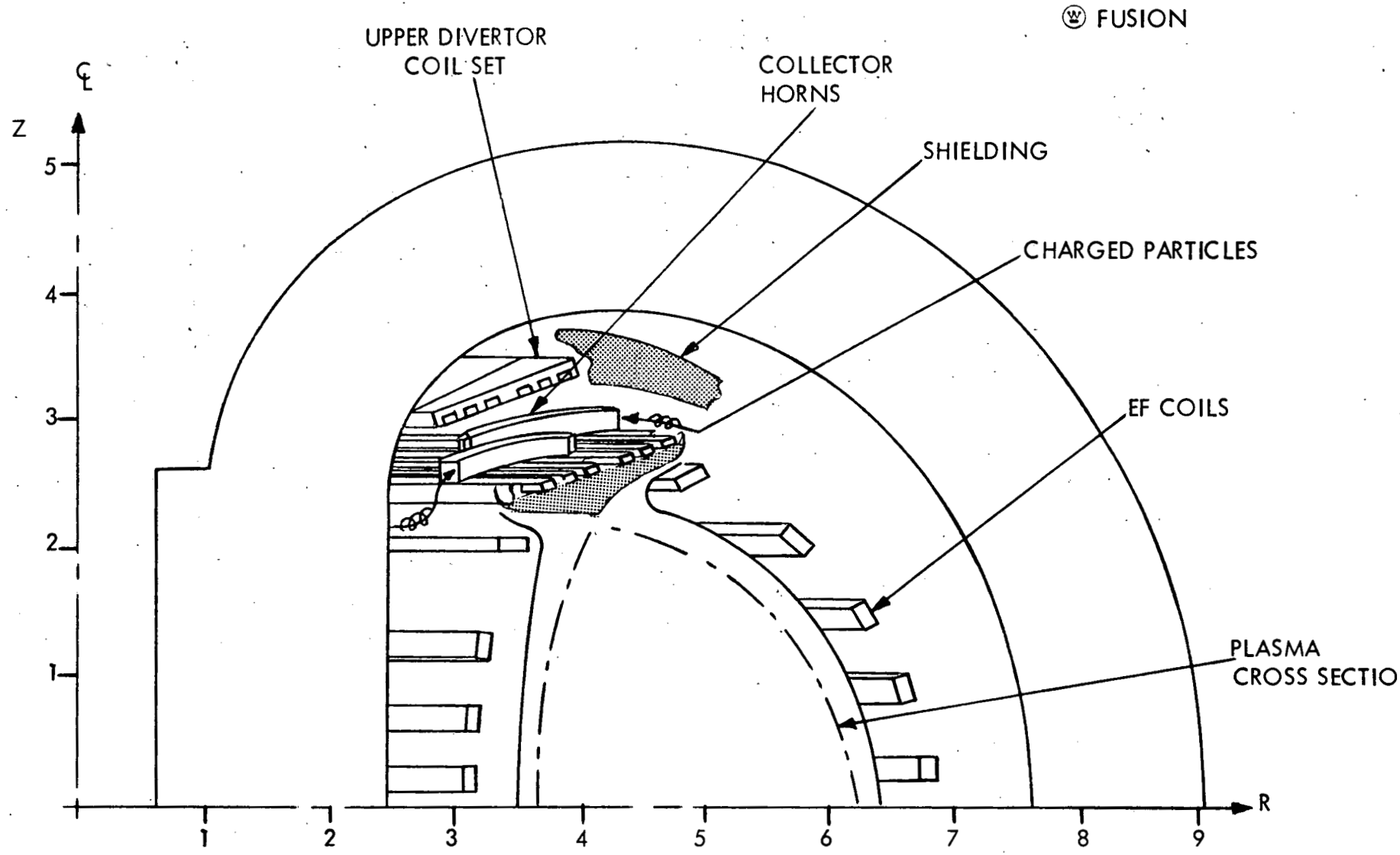

Figure 7-1. Cross-sectional view of TNS-4 when the compact divertor is included. The TNS-4 was originally designed without a divertor.

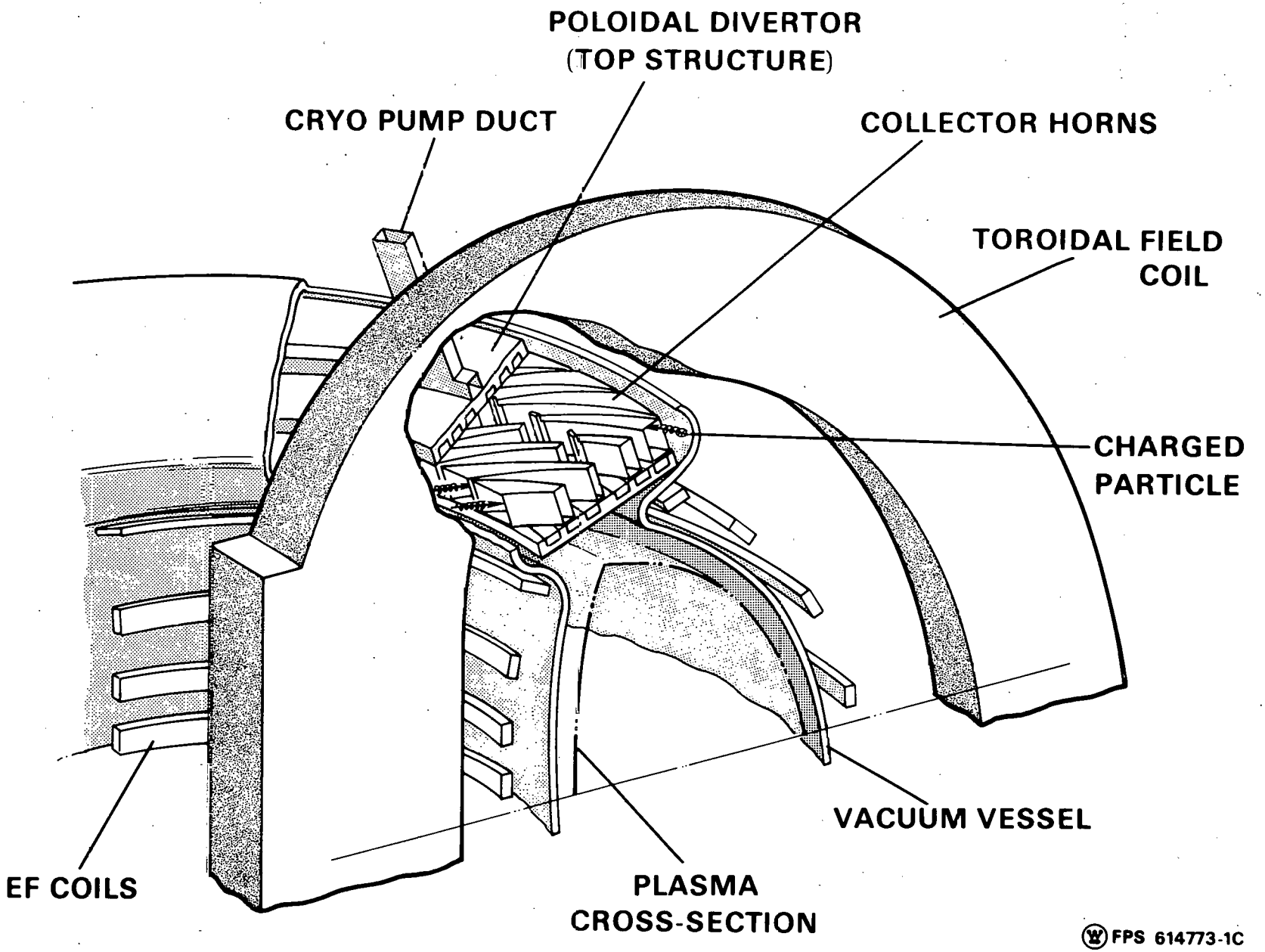

Figure 7-2. Trimetric view of TNS-4 when the compact divertor is included. The TNS-4 was originally designed without a divertor.

8.0 SUMMARY AND CONCLUSIONS

This compact poloidal divertor appears to be a viable approach from the evaluation of the major aspects discussed in this report. This design makes economical use of the space inside the TF coil array and provides for a very large particle collection surface area which suggests the feasibility of using solid metal collectors. Approximately 60% of helium ions can be trapped by solid collectors; henceforth, the auxiliary pumping requirement for helium removal is greatly reduced.

We also conclude that if the particle unload and impurity shielding effects of a poloidal divertor can be demonstrated experimentally, this divertor design would offer excellent overall characteristics as a particle removing and power handling device. Large particle collecting surface areas can be obtained and thus the power deposition and particle flux can be reduced to manageable levels. This design also appears to be feasible from the engineering point of view. The backstreaming of helium can be kept at about 20%.

In this report, only the major aspects of the divertor design issues related to TNS have been scoped. Although this design is considered feasible and offers an overall answer to the impurity control and ash removal problems, further work remains to be done. Some of the remaining design issues and experimental tasks are:

- The three dimensional magnetic field lines in the divertor burial chamber need to be calculated;
- If the lithium gravity fall is found to be desirable, theoretical and experimental studies of the characteristics of the free surface film in a strong magnetic field should be carried out. The free surface lithium $\vec{E} \times \vec{B}$ pumping in high vacuum and magnetic field has to be designed and tested;
- Lithium reprocessing technology has to be developed;

- A high speed helium pumping device has to be developed, especially for pumping a mixture of H and He;

- If the solid getter is found to be desirable, more extensive information on sticking probability, sputtering yields, and saturation dose, as functions of temperature and ion energy, have to be gathered. The ion getter pumping method has to be improved for achieving higher speed and capacity and lower sputtering yield;

- More detailed component design has to be carried out;

- Assembly, disassembly, and maintenance studies have to be carried out;

- The effects of particle impingement on the leading edges of the divertor structures must be evaluated to assure that local thermal loads and sputtering are not excessive.

The divertor engineering work performed to date has been very encouraging and it is concluded that the remaining divertor design issues for TNS are not of the GO/NO-GO variety. The compact poloidal divertor concept seems generally applicable to tokamaks; however, additional work is required to fully establish the extrapolatability of the concept to long pulse, high duty factor power reactor applications.

9.0 ACKNOWLEDGMENT

During the course of this work the continuous review and criticism of many related reports by G. Gibson and the full support of T. C. Varljen and C. A. Flanagan are acknowledged. The first author would also like to acknowledge the stimulating discussions with J. E. Faulkner, B. J. Fedor, H. J. Garber, R. E. Gold, R. R. Holman, W. J. Lange, D. A. Sink, and E. W. Sucov in many special areas such as neutronics, mechanical problems, material problems, liquid lithium properties, vacuum problems, surface physics, and chevron structures. In particular, the valuable suggestions and help on the vacuum problem by W. J. Lange are appreciated.

10.0 REFERENCE

1. Private communications with the ONRL Plasma Theory Section Staff on TNS joint studies.

2. Plasma Theory Section Staff, ORNL, Oak Ridge, Tennessee, 6th Conf. Proc. on Plasma Physics and Control Nucl. Fus. Research, IAEA-CN-35/B10, Berchtesgaden, FRG (October 1976).

3. B. Badger, et al., "Wisconsin Tokamak Reactor Design UWMAK-I," UMFDM-68, University of Wisconsin, November 1973.

4. B. Badger, et al., "Wisconsin Tokamak Reactor Design UWMAK-II," UMFDM-112, University of Wisconsin, (1975).

5. B. Badger, et al., "Wisconsin Tokamak Reactor Design UWMAK-III," UWFDM-150, University of Wisconsin, (1975).

6. B. Badger, et al., "Wisconsin Tokamak Engineering Test Reactor Design-TETR," to be published.

7. M. Yoshikawa, et al., "Research on a Tokamak with an Axisymmetric Divertor and Impurity Problems in Tokamak Devices," 5th IAEA Conference on Plasma Physics and Continual Nuclear Fusion Research (Tokyo 1974), Vol 1, 17 (Vienna 1975).

8. PDX, The Poloidal Divertor Experiment, paper No. 47, Joint Euratom-US Workshop on Large Tokamak Designs, Culham 1974.

9. T. F. Yang, "A Direct Energy Conversion Scheme for a Tokamak with a Poloidal Divertor," Bulletin of the American Physics Society, 18, 1303 (1973).

10. R. Prater, et al., "A Tokamak Divertor Experiment in the DC Octopole," 5th IAEA Conference on Plasma Physics and Continual Nuclear Fusion Research (Tokyo 1974), Vol 1, 291 (Vienna 1975).

11. F. H. Tenney, "The Divertor and Vacuum System," Chapter 6, "A Fusion Power Plant", MATT-1050, August 1974.

12. ASDEX Proposal, Part I (October 1973), Part II (June 1974).

13. A. V. Georgievsky, et al., "Conceptual Design of a Divertor for a Tokamak Experimental Power Reactor," Proceedings of the 6th Symposium on Engineering Problems of Fusion Research, San Diego, CA, November 1975, p. 583.

14. The JET Project, First Proposal, EUR-JET-R2 (April 1974).

15. M. Keilhacker, Max-Plank, IPP III/33 (November 1976).

Ⓦ FUSION

16. A. Mense, Ph D. Dissertation, University of Wisconsin (1977).

17. A. J. Mense, G. A. Emmert, J. D. Callen, N.F., 15, 703 (1975).

18. R. P. Rose, editor, "Fusion Driven Actinide Burner Design Study," Westinghouse Electric Corporation, WFPS-TME-033 (1976).

19. H. Maeda, et al., 6th Conf. Proc. on Plasma Physics and Control Nucl. Fus. Research, IAEA-CN-35/A18, Berchtesgaden, FGR (October 1976).

20. K. Ando, et al., 6th Conf. Proc. on Plasma Physics and Control Nucl. Fus. Research, IAEA-CN-33/B-44, Berchtesgaden, FRG (October 1976).

21. Annual Report of the Division of Thermonuclear Fusion Research, JAERI-M-6926 (April, 1975 to March 31, 1976).

22. A. H. Boozer, A. Rechester, "Effect of Field Errors on Divertor Scrape-Off Width," Proc. Annual Contr. Fus. Theory Conf., paper E3, San Diego (May 1977).

23. E. W. Sucov, D. K. McClain, and J. W. H. Chi, "Efficient Particle Removal from Tokamak Reactors," Trans. International Conf. on World Nucl. Energy, Washington, D.C., Vol 24, 59 (Nov. 1976) and references cited.

24. P. Y. Achemer, "Alkali Metals Evaluation Program Quarterly Report, October 1 to December 31, 1966," Aerojet General Corporation, Report AGN-8215 (1967).

25. G. McCracken and S. K. Erents, "Ion Burial In The Divertor of A Fusion Reactor," BNES Nuclear Fusion Reactor Conference, Culham, 353 (1969).

26. Y-K. M. Peng, D. J. Strickler, "Equilibrium Field Coils and Free Boundary Equilibrium Consideration for TNS," submitted to the ANS Winter Meeting in San Francisco (1977).

27. George W. Sutton, Arthur Sherman, Engineering Magnetohydrodynamics, McGraw-Hill, New York (1965).

28. M. A. Hoffman, G. A. Carlson, "Calculation Techniques for Estimating the Pressure Losses for Conducting Fluid Flows in Magnetic Fields," LLL Report UCRL-51010 (1971).

29. A. Y. Lee, "TAP-B, A General Purpose Computer Code for Coupled Heat Conduction and Hydraulic Analysis," to be published.

30. T. Baumesster, L. S. Marks, Standard Handbook for Mechanical Engineers, Seventh Edition, McGraw-Hill (1967).

31. P. A. Redhead, J. P. Hobson, and E. V. Kornelson, The Physical Basis of Ultrahigh Vacuum, Chapman & Hall, London (1967).

32. J. H. Singleton, Journal of Vacuum Science Technology, 6, 316 (1968).

33. W. J. Lange, Journal of Vacuum Science Technology, 14, 582 (1977).

34. D. L. Jassby, J. D. Lee, Proceedings US-USSR Symposium on Fusion-Fission Reactors, Conference-760733, LLL, CA (1967).

35. M. Borgi, B. Ferrario, Journal of Vacuum Science Technology, 14, 570 (1977).

36. T. F. Yang, "The Utilization of Solid Getters for Poloidal Divertor," to be published.

37. D. Lal, et al., Journal of Applied Physics, 40, 3257 (1969).

38. G. M. McCracken, J. H. C. Maple, British Journal of Applied Physics, 18, 919 (1967).

39. R. Behrisch, et al., Journal Nuclear Materials, 56, 365 (1975).

40. G. M. McCracken and D. K. Jeffries, 5th Symposium on Fusion Technology, Oxford (1968).

41. C. E. Knight and G. K. Wehner, Journal of Applied Physics, 35, 322 (1964).

42. A. Summers, N. Freeman, R. Daley, Journal of Applied Physics, 42, 4774 (1971).

43. W. Ekstein, et al., Radiation Effects, 18, 135 (1973).

44. S. A. Cohen, "Charge-Exchange Sputtering Predictions for ST and PLT," Princeton Plasma Lab., MATT-1171 (1971).

45. H. J. Halama and J. R. Aggus, Journal of Vacuum Science Technology, 11, 333 (1974).

46. J. D. Jackson, Classical Electrodynamics, 2nd Edition, John Wiley and Sons, New York (1962).

APPENDIX A
THE THEORY AND CALCULATIONAL METHOD FOR $\vec{E}$ X $\vec{B}$ PUMPS

The requirements for the design of an $\vec{E}$ X $\vec{B}$ pump system for pumping the liquid lithium out of the burial chamber of the poloidal divertor has been discussed in Section 3.1. The theory for magnetohydrodynamic channel flow in an electromagnetic field will be reviewed. The exact solutions for the pressure drop, velocity, and current distributions of the flow are obtained. The method of calculation to determine the size of the $\vec{E}$ X $\vec{B}$ pump, the electric field, the current, and the power required for pumping the lithium out of the magnetic field is discussed.

The motion of a conducting fluid in an electromagnetic field between two fixed boundaries as shown in Figure AA-1 is characterized by the magnetic Reynolds number and the Hartmann number[27,46].

$$R_m = \mu_o \bar{u} \sigma a \qquad \text{(AA-1)}$$

$$H_a = \sqrt{\frac{\sigma B_o^2 a^2}{\eta}} \qquad \text{(AA-2)}$$

Here, σ is the conductivity, η is the viscosity of the fluid, B_o is the transverse magnetic field, μ_o is the permeability and $\bar{u}$ is the average velocity. For liquids like mercury or sodium in the laboratory, $R_m < 1$, and except for very high velocities, the field lines will diffuse relative to the fluid. If $R_m >> 1$, the field lines are frozen in the fluid. In the latter case the velocity of both fluid and lines of force is the $\vec{E}$ X $\vec{B}$ drift:

$$\bar{u} = \frac{\vec{E} \times \vec{B}}{B^2} \qquad \text{(AA-3)}$$

As is shown by Figure AA-1, the magnetohydrodynamic flow between boundaries with crossed electric and magnetic fields is laminar if $H_a \to 0$. If $H_a >> 1$, the flow

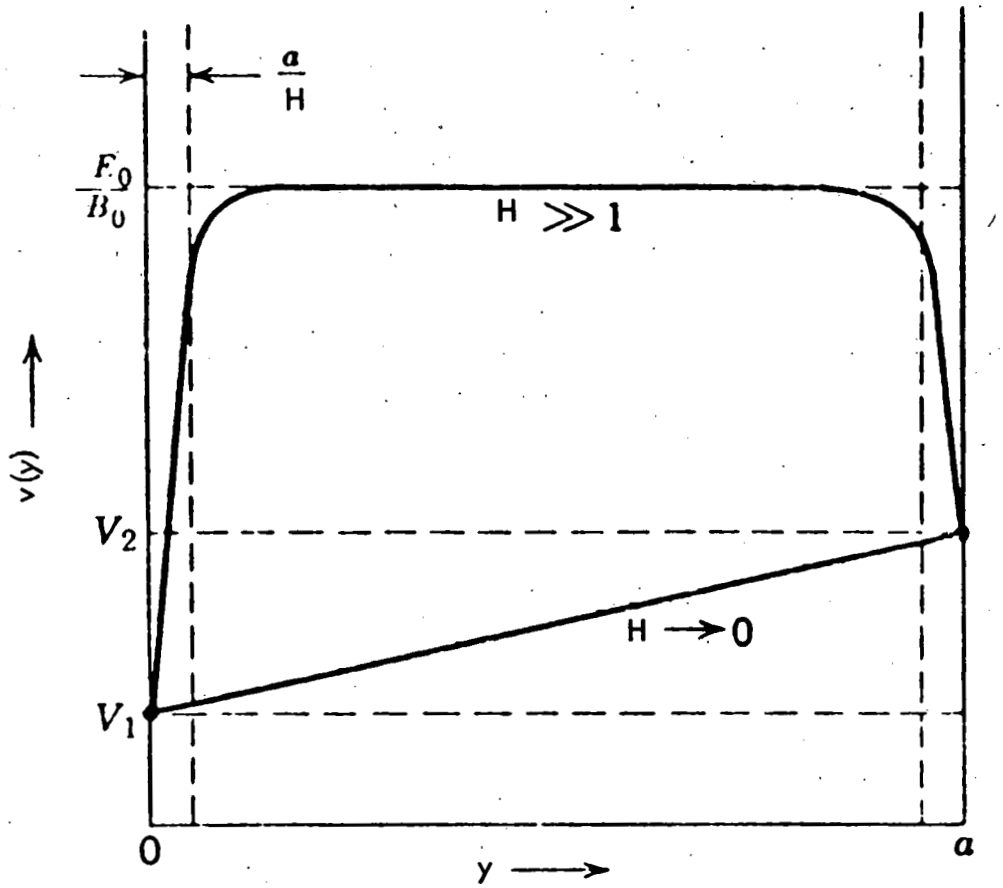

Figure AA-1. Velocity profiles for large and small Hartmann numbers, H. For H → 0, laminar flow occurs. For H >> 1, the flow is given by the $\vec{E} \times \vec{B}$ drift velocity, except in the immediate neighborhood of the boundaries.

is called Hartmann flow and the velocity is given by the $\vec{E} \times \vec{B}$ drift also, except in the immediate neighborhood of the boundaries. The expressions for velocity distribution and the relationship of the velocity and pressure gradient for Hartmann flow will be derived as follows.

The channel geometry for Hartmann flow in a uniform electromagnetic field has been shown as Figure 3-1. For simplification, the Hall effect, the end effect, and the secondary flow are neglected. The theory can be extended to include these effects when such need is warranted. The simplified theory is adequate for the present study.

The velocity, current density, magnetic field, and electric vectors are assumed to be:

$$\vec{V} = (0, 0, u) \tag{AA-4}$$

$$\vec{j} = (0, j_y, 0) \tag{AA-5}$$

$$\vec{B} = (B_o, 0, b_z) \tag{AA-6}$$

$$\vec{E} = (0, E_o, 0) \tag{AA-7}$$

where B_o and E_o are constant externally applied fields. The general equations to be solved are:

$$\text{ohm's law: } j - \sigma (\vec{E} + \vec{V} \times \vec{B}) \tag{AA-8}$$

$$\text{continuity equation: } \nabla \cdot (\rho \vec{V}) + \frac{\delta \rho}{\delta t} = 0 \tag{AA-9}$$

$$\text{equation of motion: } \rho \frac{d\vec{V}}{dt} = \vec{\nabla P} + \vec{j} \times \vec{B} + \rho \vec{g} + \eta \nabla^2 \vec{V} \tag{AA-10}$$

$$\text{Maxwell equations: } \nabla \times \vec{B} = \mu_o j \tag{AA-11}$$

$$\nabla \cdot \vec{B} = 0 \tag{AA-12}$$

$$\nabla \times \vec{E} = \frac{\delta B}{\delta t} \tag{AA-13}$$

$$\nabla \cdot \vec{E} = \frac{\rho_o}{K_o} \tag{AA-14}$$

and the boundary condition:

$$u\ (\pm\ a)\ =\ 0\ . \qquad \text{(AA-15)}$$

Here, ρ is the density and η is the viscosity of the fluid. Assuming the fluid is incompressible, and neglecting the displacement current and space charge, the Eqs. (AA-9, AA-12, AA-13, and AA-14) are satisfied. Eqs. (AA-8) and (AA-10) are reduced to:

$$j_y\ =\ \sigma\ (E_o\ -\ u\ B_o) \qquad \text{(AA-16)}$$

$$\frac{\delta p}{\delta z}\ =\ j_y\ B_o\ +\ \eta\ \frac{d^2u}{dx^2}\ +\ \rho g \qquad \text{(AA-17)}$$

and

$$\frac{\delta P}{\delta x}\ =\ -\ j_y\ b_z \qquad \text{(AA-18)}$$

Writing $P_z = \frac{\delta P}{\delta z} - \rho g$ and combining Eqs. (AA-16) and (AA-17), one finds:

$$\eta\ \frac{d^2u}{dx^2}\ -\ \sigma\ B_o^{\,2}\ u\ -\ P_z\ +\ \sigma\ B_o\ E_o\ =\ 0 \qquad \text{(AA-19)}$$

Let

$$\bar{u}\ =\ \frac{1}{2a}\ \int_{-a}^{a}\ -\ u dx$$

which is a measure of the mass flow. Introducing the following dimensionless variables:

$$U\ =\ \frac{u}{\bar{u}} \qquad Z\ =\ \frac{z}{a} \qquad X\ =\ \frac{x}{a}$$

$$K\ =\ \frac{E_o}{\bar{u}\ B_o} \qquad P\ =\ \frac{p}{\rho \bar{u}^{\,2}} \qquad \tilde{b}_x\ =\ \frac{b_x}{B_o\ R_m} \qquad \text{(AA-20)}$$

$$H_a^{\,2}\ =\ \frac{\sigma\ B_o^{\,2}\ a^2}{\eta} \qquad R_e\ =\ \frac{\rho \bar{u} a}{\eta} \qquad R_m\ =\ \mu_o\ \bar{u}\ \sigma\ a$$

Equation (AA-19) becomes

$$\frac{d^2 \bar{U}}{dZ^2} - H_a^2 U - R_e P_z + K H_a^2 = 0 \qquad \text{(AA-21)}$$

with boundary conditions of

$$U (\pm 1) = 0. \qquad \text{(AA-22)}$$

The solution for U is found to be

$$U = (K - \frac{R_e P_z}{H_a^2}) \frac{\cosh H_a - \cosh H_a X}{\cosh H_a} . \qquad \text{(AA-23)}$$

Taking the average value of U, one obtains the relationship

$$K - \frac{R_e P_z}{H_a^2} = \frac{H_a}{H_a - \tanh H_a} \qquad \text{(AA-24)}$$

Then, the velocity distribution, Eq. (AA-23), becomes

$$U = \frac{H_a (\cosh H_a - \cosh H_a X)}{H_a \cosh H_a - \sinh H_a} \qquad \text{(AA-25)}$$

From Eq. (AA-16), the normalized current density $J_y = j_y/\sigma B_o \bar{u}$ is simply

$$J_y (X) = K - U (X). \qquad \text{(AA-26)}$$

The normalized current per unit channel length flowing through the external circuit is given by

$$J = \int_{-1}^{+1} J_y \, dx = 2 (K - 1) \qquad \text{(AA-27)}$$

The characteristics and the application of Eqs. (AA-23 through AA-27) will be discussed in the next section.

Method of Calculation. If the channel flow is Hartmann, the velocity distribution given by Eq. (AA-25) is shown by the solid curve in Figure AA-2. The current distribution by Eq. (AA-26) for K = 2 is shown by the dashed curve.

From Eq. (AA-24) the pressure gradient can be written as

$$P_z = \frac{H_a^2}{R_e} (K - P_m) \qquad \text{(AA-28)}$$

where P_m is the pressure drop factor due to magnetic viscosity and is

$$P_m = \frac{H_a}{H_a - \tanh H_a} \qquad \text{(AA-29)}$$

The normalized power density can be written as

$$W = KJ = 2K(K - 1) \qquad \text{(AA-30)}$$

The averaged current density, power density, and pressure gradient are plotted as functions of K in Figure AA-3. We notice that $P_z = J = W = 0$ at $K = 1$. This corresponds to an open circuit. The current is positive and is supplied by an external power supply for $K > 1$. This is the case of an MHD accelerator or pump where the pressure gradient is positive. The current is negative when $K < 1$ and the channel can be used as a flow meter.

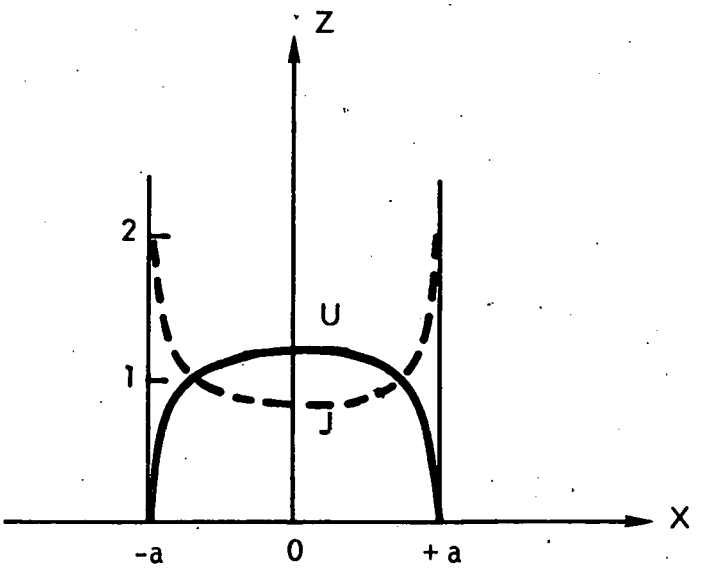

Figure AA-2. Velocity and current distribution for Hartmann flow, $H_a >> 1$.

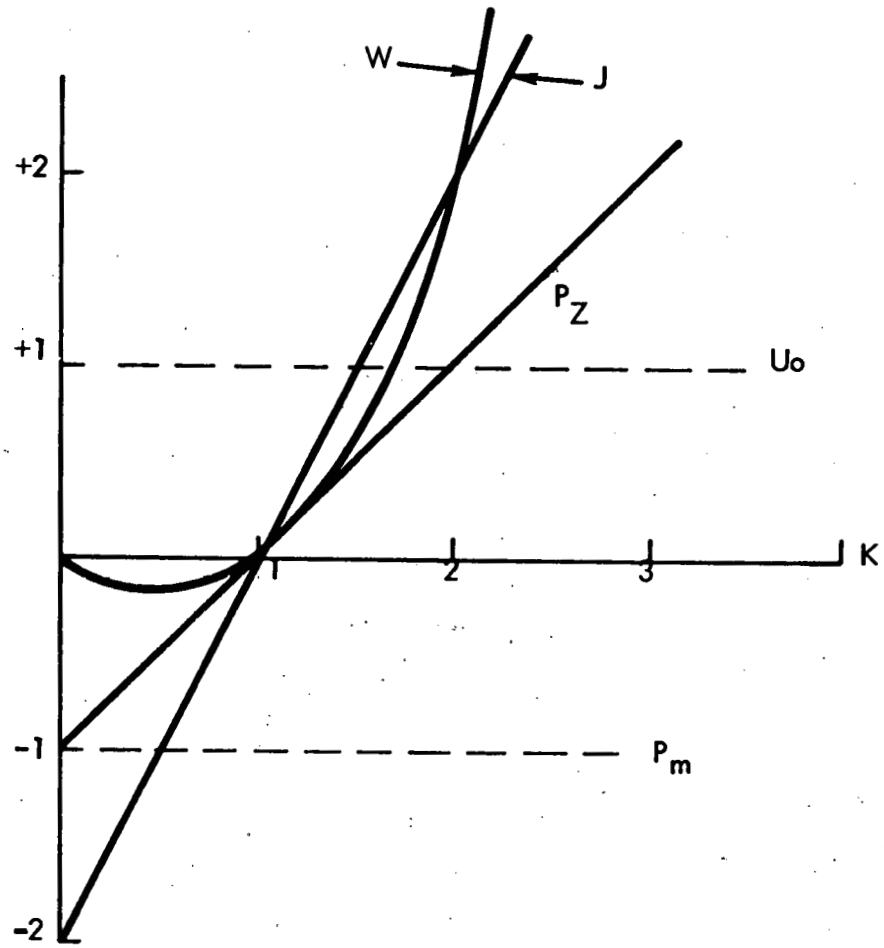

Figure AA-3. Current, power, and pressure distributions.

INTERNAL DISTRIBUTION

1. J. H. Fink
2. C. A. Flanagan
3. J. W. French
4. G. Gibson
5. D. J. Grove
6. G. W. Hardigg
7. F. M. Heck
8. J. L. Johnson
9. A. R. Jones
10. C. K. Jones
11. J. S. Karbowski
12. D. Klein
13. W. P. Kovacik
14. G. A. Krist
15. I. Liberman
16. R. P. Rose
17. Z. M. Shapiro
18. C. C. Sterrett
19. R. W. Stooksberry
20. T. C. Varljen
21. R. W. Warren
22. P. N. Wolfe
23. J. L. Young

24-37. Fusion Library

38-39. ARD Library

OAK RIDGE NATIONAL LABORATORY DISTRIBUTION

40. J. F. Clarke
41. P. N. Haubenreich
42. O. B. Morgan
43. Y-K. M. Peng

44-58. M. Roberts

59. M. W. Rosenthal
60. T. E. Shannon
61. D. Steiner
62. D. W. Swain

EXTERNAL DISTRIBUTION

63. J. L. Anderson, Los Alamos Scientific Laboratory, P. O. Box 1663, Los Alamos, NM 87545.
64. D. J. Anthony, General Electric Co., Schenectady, NY 12345.
65. C. C. Baker, General Atomic Co., San Diego, CA 92138.
66. A. A. Bishop, Nuclear Engineering Programs Director, Chemical Engineering Department, University of Pittsburgh, Pittsburgh, PA 15261.
67. S. L. Bogart, Energy Research and Development Administration, Division of Magnetic Fusion Energy, Mail Stop G-234, Washington, DC 20545.
68. S. J. Buchsbaum, Bell Laboratories, Crawford Corner Road, Holmdel, NJ 07733.
69. R. W. Bussard, Energy Resources Group, Inc., 1500 Wilson Blvd., Suite 505, Arlington, VA 22209.
70. Yung-An Chao, Nuclear Science and Engineering Div., Carnegie-Mellon University, Schenley Park, Pittsburgh, PA 15213.
71. R. N. Cherdack, Burns & Roe, Inc., 283 Highway 17, Paramus, NJ 07652.
72. F. E. Coffman, Energy Research and Development Administration, Division of Magnetic Fusion Energy, Mail Stop G-234, Washington, DC 20545.
73. D. R. Cohn, Francis Bitter Laboratory, MIT, 120 Albany St., Cambridge MA 02139.
74. R. W. Conn, Nuclear Engineering Dept., University of Wisconsin, Madison, WI 53706.
75. E. C. Creutz, National Science Foundation, 1800 G Street, N.W., Washington, DC 20440.

76. H. S. Cullingford, Energy Research and Development Administration, Division of Magnetic Fusion Energy, Mail Stop G-234, Washington, DC 20545.
77. R. C. Davidson, U.S. Energy Research and Development Administration, Division of Magnetic Fusion Energy, Mail Stop G-234, Washington, DC 20545.
78. N. A. Davies, Energy Research and Development Administration, Division of Magnetic Fusion Energy, Mail Stop G-234, Washington, DC 20545.
79. S. O. Dean, Energy Research and Development Administration, Division of Magnetic Fusion Energy, Mail Stop G-234, Washington, DC 20545.
80. A. Favale, Grumman Aerospace Corp., Bethpage, NY 11714.
81. S. Fernback, Lawrence Livermore Laboratory, Livermore, CA 94551.
82. E. von Fischer, Bechtel Corp., P. O. Box 3965, San Francisco, CA 94119.
83. H. K. Forsen, Exxon Nuclear Co., 777 106th Ave. N.E., Bellevue, WA 98004.
84. T. K. Fowler, University of California, Lawrence Radiation Laboratory, P. O. Box 808, Livermore, CA 94551.
85. H. P. Furth, Princeton Plasma Physics Laboratory, Princeton University, P. O. Box 451, Princeton, NJ 08540.
86. M. B. Gottlieb, Princeton Plasma Physics Laboratory, Princeton University, P. O. Box 451, Princeton, NJ 08540.
87. W. C. Gough, Electric Power Research Institute, Palo Alto, CA 94304.
88. J. Nelson Grace, Energy Research and Development Administration, Division of Magnetic Fusion Energy, Mail Stop G-234, Washington, DC 20545.
89. R. Harder, General Atomic Co., P. O. Box 81608, San Diego, CA 92138.
90. C. D. Henning, Energy Research and Development Administration, Division of Magnetic Fusion Energy, Mail Stop G-234, Washington, DC 20545.
91. G. K. Hess, Jr., Division of Magnetic Fusion Energy, U.S. Energy Research and Development Administration, Washington, DC 20545.
92. A. G. Hill, Plasma Fusion Center, Room 4-232, Massachusetts Institute of Technology, 77 Massachusetts Avenue, Cambridge, MA 20139.
93. R. L. Hirsch, Exxon Nuclear Corp., RM. 4330, 1251 Avenue of the Americas, New York, NY 10020.
94. T. Kammash, The University of Michigan, College of Engineering, Dept. of Nuclear Engineering, Ann Arbor, MI 48109.
95. E. E. Kintner, Energy Research and Development Administration, Division of Magnetic Fusion Energy, Mail Stop G-234, Washington, DC 20545.
96. G. Kulcinski, Nuclear Engineering Dept., University of Wisconsin, Madison WI 53706.
97. D. Kummer, McDonnell Douglas, P. O. Box 516, St. Louis, MO 63166.
98. V. A. Maroni, Argonne National Laboratory, 9700 S. Cass Ave., Argonne, IL 60439.
99. D. M. Meade, Princeton Plasma Physics Laboratory, Princeton University, P. O. Box 451, Princeton, NJ 08540.
100. G. H. Miley, Nuclear Engineering Program, 214 Nuclear Engineering Laboratory, University of Illinois, Urbana, IL 61801.
101. R. Mills, Princeton Plasma Physics Laboratory, Princeton University, P. O. Box 451, Princeton, NH 08540.
102. K. Moses, Energy Research and Development Administration, Division of Magnetic Fusion Energy, Mail Stop G-234, Washington,DC 20545.
103. M. R. Murphy, Energy Research and Development Administration, Division of Magnetic Fusion Energy, Mail Stop G-234, Washington, DC 20545.
104. S. Naymark, Nuclear Services Corp., 1700 Dell Ave., Campbell, CA 95008.
105. J. O. Neff, Energy Research and Development Administration, Division of Magnetic Fusion Energy, Mail Stop G-234, Washington, DC 20545.
106. T. Ohkawa, General Atomic Co., P. O. Box 608, San Diego, CA 92112.
107. J. Powell, Brookhaven National Laboratory, Upton, Long Island, NY 11973.
108. J. R. Purcell, General Atomic Co., P. O. Box 608, San Diego, CA 92112.

109. P. J. Reardon, Princeton Plasma Physics Laboratory, Princeton University, P. O. Box 451, Princeton, NJ 08540.
110. D. J. Rose, Department of Nuclear Engineering, Massachusetts Institute of Technology, Cambridge, MA 02139.
111. P. Sager, General Atomic Co., P. O. Box 608, San Diego, CA 92112.
112. G. A. Sawyer, Los Alamos Scientific Laboratory, P. O. Box 1663, Los Alamos, NM 87545.
113. L. C. Schmid, Pacific Northwest Laboratories, Battelle Blvd., P. O. Box 999, Richland, WA 99352.
114. M. A. Schultz, Nuclear Engineering Department, The Pennsylvania State University, 231 Sackett Building, University Park, PA 16802.
115. Weston M. Stacey, Jr., Georgia Institute of Technology, Atlanta, GA 30332.
116. C. M. Stickley, Division of Laser Fusion, U.S. Energy Research and Development Administration, Washington, DC 20545.
117. C. E. Taylor, Lawrence Livermore Laboratory, Mail Code L-384, P. O. Box 808, Livermore, CA 94550.
118. V. Teofilo, Pacific Northwest Laboratories, Battelle Blvd., P. O. Box 999, Richland, WA 99352.
119. K. Thomassen, Lawrence Livermore Laboratory, P. O. Box 808, Livermore, CA 94550.
120. B. Twining, Energy Research and Development Administration, Division of Magnetic Fusion Energy, Mail Stop G-234, Washington, DC 20545.
121. A. W. Trivelpiece, Engineering and Research, Maxwell Laboratories, Inc., 9244 Balboa Avenue, San Diego, CA 92123.
122. J. M. Williams, Energy Research and Development Administration, Division of Magnetic Fusion Energy, Mail Stop G-234, Washington, DC 20545.
123. H. H. Woodson, Department of Electrical Engineering, University of Texas, Austin, TX 78712.
124. H. Yoshikawa, Westinghouse Hanford Co., P. O. box 1970, Richland, WA 99352.
125. K. Zwilski, Energy Research and Development Administration, Division of Magnetic Fusion Energy, Mail Stop G-234, Washington, DC 20545.
126. Energy Research and Development Administration, Technical Information Center, P. O. Box 62, Oak Ridge, Tennessee 37830.
127 Doynikov, N. I., USSR; Leningrad, 188631, NIIEFA.
128 Kolbasor, B. N., Kurchatov Sq., Kurchatov Institute, USSR; Moscow, 123182
129 Karl H. Schmitter, Max-Planck Institut fur Plasmaphysik, 8046 Garching Bei Munchen, Germany.
130 Dr. A. Knobloch, Max-Planch Institut fur Plasmaphysik, D-8046 Garching Bei Munchen, Germany
131 Kiyoshi Sako, Fusion Reactor System Laboratory, Div. of Thermonuclear Fusion Research, JAERI, Tokai-mura, Maka-gun, Ibaraki-ken, Japan
132 J. T. D. Mitchell, UKAEA Culham Laboratory, Abingdon, Oxfordshire OX14 3DB, United Kingdom